CHARACTERIZATION OF THE LIQUID FILM DISTRIBUTION IN HORIZONTAL TWO-PHASE ANNULAR FLOW

Department of Industrial Engineering,
University of Napoli "Federico II"

PhD Dissertation

Filippo Cataldo

Supervisor:
Prof. Rita Mastrullo

Co-supervisors:
Prof. Alfonso William Mauro
Prof. Rémi Revellin

2015

The doctoral grant has been financed by:

- - PROGETTO POLIGRID ”Smart Grid con Sistemi di Poligenerazione Distribuita”, POR Campania FSE 2007/2013, Asse IV, Asse V, Avviso Pubblico per lo sviluppo di Reti di Eccellenza tra Universitá, Centri di Ricerca e Imprese, A.G.C. 06 D.D. n. 414 del 13.11.2009 Codice Ufficio 4-17-2, CUP B65B09000020007 - -

Contents

List of Figures

List of Tables

Nomenclature

A	area $[m^2]$
c	correction factor
D	tube diameter $[m]$
E	entrainment rate $[-]$
d	differential
Fr	Froude number $[-]$
f	friction factor $[-]$
G	mass flux $[kg/(m^2 \cdot s)]$
g	gravitational acceleration 9.81 $[m^2/s]$
h	enthalpy $[J/(kg \cdot K)]$, heat transfer coefficient $[W/(m^2 \cdot K)]$
INT	intermittency $[-]$
$iter$	interation
J	superficial velocity $[m/s]$
k	generic unknown, thermal conductivity $[W/(m \cdot K)]$
LF	laminar fraction
MRE	maximum relative error
MRR	maximum relative residual
$\dot{m}$	mass flow rate $[kg/s]$
$\dot{m}^+$	dimensionless mass flow rate $[-]$
Nu	Nusselt number $[-]$
p	pressure $[Pa]$
$P20$	Percentage of experimental data captured within ±20%
$P30$	Percentage of experimental data captured within ±30%
Pr	Prandtl number $[-]$
$\dot{Q}$	thermal power $[W]$
$\dot{q}$	heat flux $[W/m^2]$
R	tube radius $[m]$
Re	Reynolds number $[-]$
RR	relative roughness $[-]$
RME	relative mean error
r	vapour core radius $[m]$
SR	system residual
T	temperature $[°\mathrm{C}]$
T^+	dimensionless temperature $[-]$
u	axial velocity $[m/s]$

u^+	dimensionless velocity $[-]$
v	tangential velocity $[m/s]$
x	vapour quality, thermodynamic quality $[-]$
y	distance from the wall [-]
y^+	dimensionless distance from the wall

Subscripts

a	average
b	bottom
$core$	vapour core
ht	heat transfer
i	liquid-vapour interface
L	liquid phase
LF	liquid film
LFC	critical liquid film
LE	liquid entrainment
LV	liquid-vapour phase change
LW	liquid-wall
ref	reference
t	top, thermal
V	vapour phase
z	axial direction

Greek letters

γ	principal radius of curvature $[m]$
δ	liquid film thickness $[m]$
δ^+	dimensionless liquid film thickness $[m]$
ϵ	eddy diffusivity $[m^2/s]$
ϵ^+	dimensionless eddy diffusivity $[-]$
θ	tangential direction
κ	curvature $[m^{-1}]$
μ	dynamic viscosity $[Pa \cdot s]$
ν	cinematic viscosity $[m^2/s]$
ρ	density $[kg/m^3]$
σ	surface tension $[N/m]$
τ	shear stress $[N/m^2]$

Chapter 1

INTRODUCTION

According to the International Energy Agency statistic data [1], the world electricity production is strongly dependent on fossil fuels, like coal, oil and natural gas. In Fig. 1.1, the percent contribution of each source is reported. Sustainable resources, like solar, geothermal and waste heat, still need a larger application.

The challenge of reducing the consumption of fossil fuels and the growing attention in environmental concerns have lead to the development of energy conversion systems able to satisfy such needs. However, the aforementioned sustainable resources occur at a temperature significantly lower than fossil fuels. The energy conversion of such resources by means of traditional steam power cycle is not efficient and feasible. In Table 1.1, a subdivision of sustainable heat sources by grade of temperature is reported, according to Tchanche et al. [2].

The Organic Rankine cycle (ORC) is proving to be one of the most promising technologies for conversion of low-grade temperature heat sources, such as solar, geothermal and industrial waste heat. Moreover, it allows the energy conversion with adaptability to the heat source, reasonable investment cost, for small scale and distribuited power generation systems.

In recent years, the research has devoted many studies to the thermodynamic of Organic Rankine cycle, as for instance: Hung et al. [3], Borsukiewicz-Gozdur and Nowak [4], Chen et al. [5], Papadopoulos et al. [6], Quoilin et al. [7], Aneke et al. [8], He et al. [9],

°C	Solar	Geothermal	Biomass	Industrial waste
Low grade	< 80	< 100	–	< 230
Medium grade	$80 - 300$	$100 - 180$	< 350	$230 - 650$
High grade	> 300	> 180	–	> 650

Table 1.1: Subdivision by grade of heat sources.

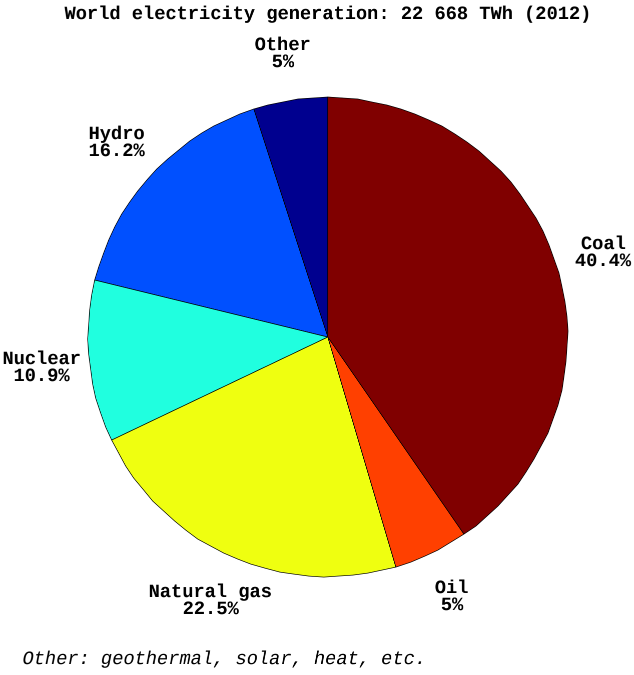

Figure 1.1: Share of resources to electricity generation.

Bao and Zhao [10], Cataldo et al. [11], Tchanche et al. [2].

A basic Organic Rankine cycle is shown in Fig. 1.2, using the working fluid R245fa. In such a cycle, it is possible to recognize the fundamental transformations of a power cycle:

- compression of the liquid flow;
- liquid heating and evaporation;
- expansion of the vapour flow;
- desuperheating and condensation.

Because of the low values of temperature of the heat sources, the reduction of thermal entropy generation in the heat exchangers is crucial. It is well-known that the larger the mean temperature difference between the fluids in heat exchangers, the greater the thermal entropy generation. In Fig. 1.3, the temperaure variations are reported against the cumulative heat exchanged for the R245fa cycle.

The relationship between fluid temperature and heat flow is gven in Eq. (1.1), for an infinitesimal control volume:

$$\mathrm{d}\dot{Q} = U(T_{\mathrm{hot}} - T_{\mathrm{cold}})\mathrm{d}A_{\mathrm{ht}} \tag{1.1}$$

where U is the overall heat transfer coefficient and $\mathrm{d}A_{\mathrm{ht}}$ is the infinitesimal heat transfer area.

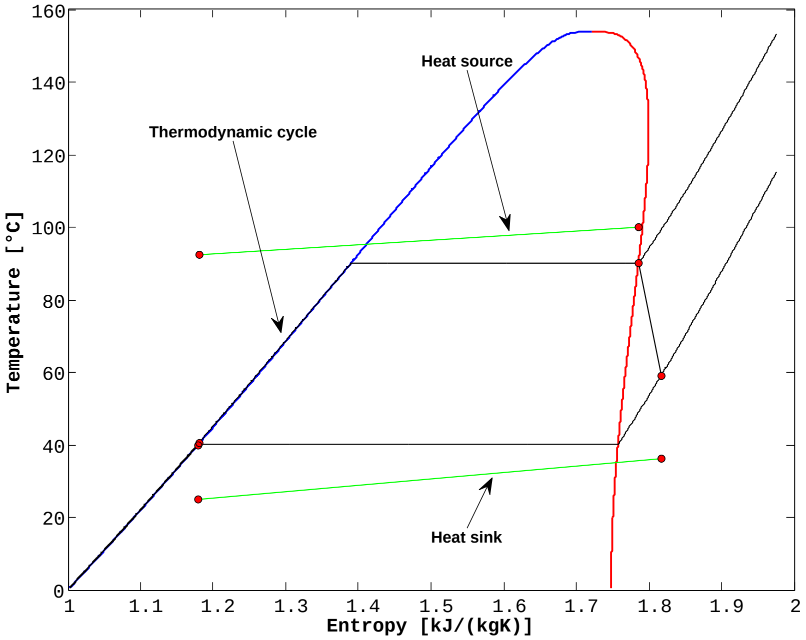

Figure 1.2: Basic organic Rankine cycle with R245fa as working fluid.

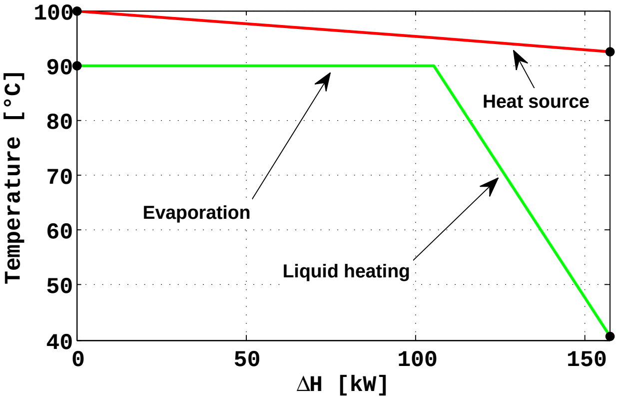

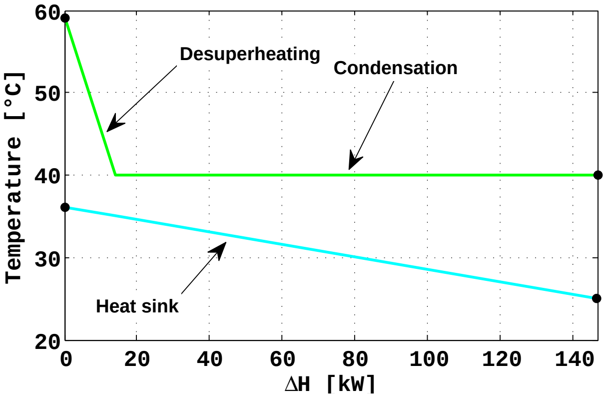

Figure 1.3: Temperature variations in the heat exchangers for R245fa cycle.

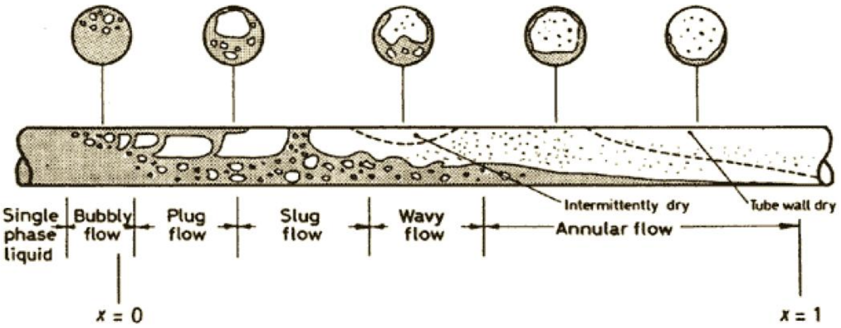

Figure 1.4: Flow patterns in horizontal tubes during evaporation.

In order to realise a better temperature matching, a proper heat exchanger design is meant to increase the overall heat transfer coefficient. However, it should be noted that pressure drop occurs in fluid flows, according to the force balance in Eq. (1.2):

$$\frac{\mathrm{d}p}{\mathrm{d}z} = -\frac{4}{D}\tau \tag{1.2}$$

Pressure drops are the cause for mechanical entropy generation. The heat transfer coefficient and the pressure drop compete on varying the operational conditions and geometry in heat exchangers. Therefore, it is essential the knowledge of methods able to calculate such quantities.

In two-phase flow, the fluid flow and heat transfer predictions are complicated because of the relative configuration assumed by the liquid and the vapour phases, namely the flow pattern. References about two-phase flow patterns can be found in Kattan et al. [12], Zürcher et al. [13], El Hajal et al. [14], Wojtan et al. [15, 16], Mastrullo et al. [17], Kim and Mudawar [18], Charnay et al. [19]. The most usual flow pattern encountered in evaporation and condensation processes in horizontal tubes are:

- bubbly flow;
- plug flow;
- slug flow;
- wavy flow;
- annular flow.

In Fig. 1.4, a representation of flow patterns occurring in a horizontal tube during evaporation is shown (Collier and Thome [20]).

It is worth noting that the occurrence of a particular flow pattern depends on the operational conditions, the thermodynamic quality and the channel size. A flow pattern map describes the range of conditions in which the flow patterns occurs. In Fig. 1.5, a flow pattern map from Wojtan et al. [15] is derived for evaporating R245fa at saturation temperature of 70 °C.

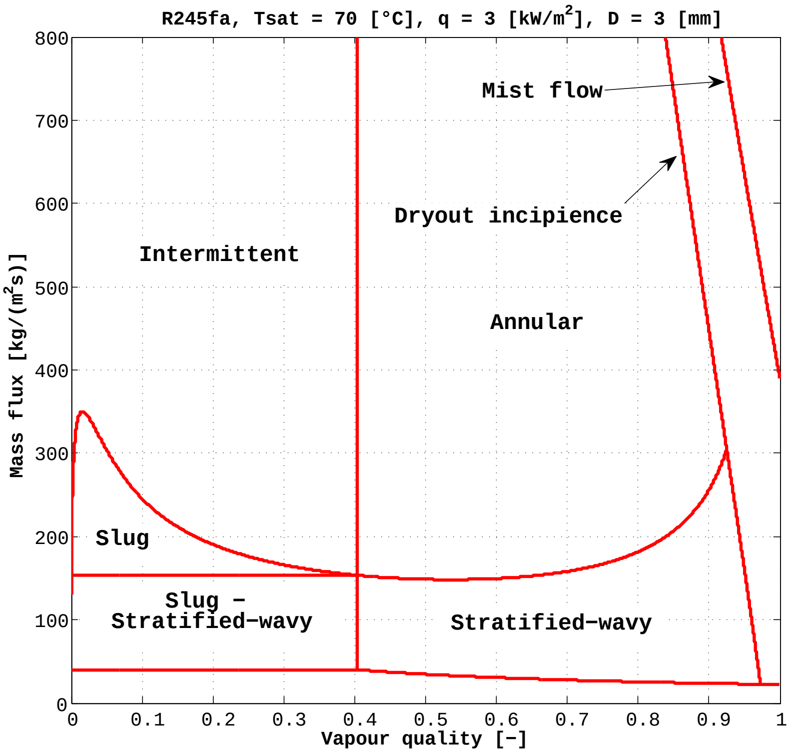

Figure 1.5: Flow pattern map for evaporating R245fa, using the transition lines from.

The annular flow pattern play an important role in two-phase heat transfer: causes very high values of heat transfer coefficient and affects the dryout condition. The annular flow is characterised by a thin liquid film, which completely or partially wets the pipe wall, and a vapour core flowing in the centre. The liquid phase may flow as *entrained droplets* in the vapour core. The liquid droplets mass flow rate derives from a competition between deposition rate and entrainment rate. An important feature of the liquid-vapour interface is the presence of dynamic waves, usually discerned in *disturbance waves* of large amplitude and *ripples* of low amplitude. The thinness of the liquid film ensures an enhanced convection respect to the liquid single-phase flow. However, it is also responsible for an early dryout and, hence, an abrupt decrease of heat transfer. A comprehensive literature about the annular flow can be found in Wallis [21], Hewitt and Hall-Taylor [22], Hanratty [23], Whalley [24], and Collier and Thome [20].

The purpose of this study is an in-depth analysis of the annular flow in order to propose a two-dimensional model able to predict the cross-sectional liquid film distribution. Indeed, such a distribution may cause a significant variation of the heat transfer coefficient from the tube top toward the tube bottom. The cross-sectional variation of the heat transfer coefficient is not taken into account by one-dimensional models and correlations and, therefore, an improper heat exchanger design may be originated. In literature, several studies are present about the topic. Bar-Cohen et al. [25, 26] stated that the minimization of the wall temperature difference around the pipe circumference occurs at the onset of the annular flow. Jayanti and Hewitt [27] analysed a vertical liquid film induced by upward gas flow by means of a numerical two-dimensional CFD model. They highlighted the enhancement of the heat transfer due to the disturbance waves, which are packets of turbulence transported by the vapour phase along the tube. Hetsroni et al. [28] obtained measurements of the heat transfer coefficient for air-water flow along the pipe circumference in a upward inclined tube. The same task has been performed by Zimmerman et al. [29] in a 25 mm diameter horizontal tube by means of infrared thermography technique. They showed an higher heat transfer coefficient at the tube bottom because of the augmentation of the turbulence at higher film thickness. This behaviour was mainly due to two phenomena: the waviness of the liquid-vapour interface and the entrainment of vapour bubbles in the liquid film.

Chapter 2

STATE-OF-ART OF ANNULAR FLOW MODELLING

2.1 Prediction of the liquid film thickness

2.1.1 The triangular relationship

Assuming that the liquid film behaves like a boundary layer region in single-phase flow, the universal velocity profile can be used, as reported by Whalley [24].

$$u^+ = f(y^+) \tag{2.1}$$

where the dimensionless velocity u^+ and the dimensionless distance from the wall y^+ are given by the Eqs. (2.2) and (2.3).

$$u^+ = u\left(\frac{\rho_\mathrm{L}}{\tau}\right)^{0.5} \tag{2.2}$$

$$y^+ = y\left(\frac{\tau}{\rho_\mathrm{L}}\right)^{0.5}\frac{\rho_\mathrm{L}}{\mu_\mathrm{L}} \tag{2.3}$$

According to the turbulence theory, the universal velocity profile can be calculated by the following expression:

$$u^+ = \begin{cases} \text{laminar sublayer:} & y^+, & \text{for } y^+ < 5; \\ \text{buffer layer:} & -3.05 + 5\ln(y^+), & \text{for } 5 < y^+ < 30; \\ \text{turbulent core:} & 5.5 + 2.5\ln(y^+), & \text{for } y^+ > 30. \end{cases} \tag{2.4}$$

Usually, in liquid-vapour annular flow, the liquid film thickness δ is small compared to the channel diameter D. Under this assumption, the liquid film flow rate $\dot{m}_\mathrm{LF}$ can be found by integrating the velocity profile:

$$\dot{m}_\mathrm{LF} = \pi D \int_o^\delta \rho_\mathrm{L} u \,\mathrm{d}y \tag{2.5}$$

Using Eqs. (2.2) and (2.3), the following dimensionless equation can be obtained:

$$\dot{m}_{\mathrm{LF}}^{+} = \int_{o}^{\delta^{+}} u^{+}\,\mathrm{d}y^{+} \tag{2.6}$$

where

$$\dot{m}_{\mathrm{LF}}^{+} = \frac{\dot{m}_{\mathrm{LF}}}{\pi D \mu_{\mathrm{L}}} \tag{2.7}$$

$$\delta^{+} = \delta \left(\frac{\tau}{\rho_{\mathrm{L}}}\right)^{0.5} \frac{\rho_{\mathrm{L}}}{\mu_{\mathrm{L}}} \tag{2.8}$$

Solving the integral in Eq. (2.6) with the universal velocity profile given in Eq. (2.4), the *triangular relationship* is finally achieved.

$$\dot{m}_{\mathrm{LF}}^{+} = \begin{cases} 0.5\delta^{+}, & \text{for } \delta^{+} < 5; \\ 12.5 - 8.05\delta^{+} + 5\delta^{+}\ln(\delta^{+}), & \text{for } 5 < \delta^{+} < 30; \\ -64 + 3\delta^{+} + 2.5\delta^{+}\ln(\delta^{+}), & \text{for } \delta^{+} > 30. \end{cases} \tag{2.9}$$

It is worth mentioning that, according to the annular flow theory, the shear stress in the liquid film is almost uniform and equal to the interfacial shear stress. Therefore in Eqs. (2.2) and (2.3), the interfacial shear stress τ_i is used and calculated with a proper correlation, unless otherwise stated. Owen and Newell [30], Hurlburt and Newell [31], Shedd [32] used the universal velocity profile showing a satisfactory agreement against experimental data. Dobran [33, 34] stated that the turbulence is reduced near the liquid-vapour interface. The two-layer model proposed by Dobran showed a better agreement for very thin liquid film. Cioncolini et al. [35] recommended the simultaneous application of the universal velocity profile and the Dobran's model, and carried out a new simple turbulence model which seems to be the best predictive method so far.

2.1.2 Liquid film thickness correlations

It is usual to define a liquid film Reynolds number as:

$$Re_{\mathrm{LF}} = \frac{4\dot{m}_{\mathrm{LF}}}{\pi D \mu_{\mathrm{L}}} \tag{2.10}$$

where $\dot{m}_{\mathrm{LF}}$ is liquid mass flow rate flowing in the liquid film and D is channel diamater. Assuming the liquid film thickness δ small relative to the channel diameter, the liquid Reynolds number can be computed as follows:

$$Re_{\mathrm{LF}} = \frac{4\rho_{\mathrm{L}} u_{\mathrm{LF}} \delta}{\mu_{\mathrm{L}}} \tag{2.11}$$

It should be noted that both the mass flow rate and the velocity of the liquid film are calculated assuming the entrainment rate $\dot{m}_{\mathrm{LE}}$ known. From the definition of the entrainmet ratio E,

$$E = \frac{\dot{m}_{\mathrm{LE}}}{\dot{m}_{\mathrm{L}}} \tag{2.12}$$

the liquid film mass flow rate is given by the following:

$$\dot{m}_{\mathrm{LF}} = \dot{m}_{\mathrm{L}}(1 - E) \tag{2.13}$$

Among the first authors to propose a correlation for the liquid film thickness, Kosky [36] found the following correlation for the dimensionless film thickness, solving a force balance on the liquid film with a turbulent velocity profile for vertical upward flows:

$$\delta^+ = \begin{cases} (2Re_{\mathrm{LF}})^{0.5}, & \text{if } \delta^+ < 25; \\ 0.0512Re_{\mathrm{LF}}^{-0.875}, & \text{if } \delta^+ > 25. \end{cases} \tag{2.14}$$

Ishii and Gromels [37], assuming the roll-wave as the predominant mechanism for the entrainment of liquid droplet [38], derived the following criterion by considering a force balance between the vapour drag force on a wave crest and the surface tension.

$$\delta^+ = 0.347Re_{\mathrm{LF}}^{2/3} \tag{2.15}$$

Asali et al. [39] correlated the dimensionless film thickness against the liquid film Reynolds number in the ripple regime, as reported in Eq. (2.16).

$$\delta^+ = 0.34Re_{\mathrm{LF}}^{0.6} \tag{2.16}$$

They found that, for vertical air-water flows, the ripple regime stands for $Re_{\mathrm{LF}} < 300$. Henstock [40] proposed the Eq. (2.17) for the disturbance wave regime.

$$\delta^+ = 0.0379Re_{\mathrm{LF}}^{0.9} \tag{2.17}$$

Hurlburt and Newell [31] proposed a combination between Asali's and Henstock's correlations in order to predict the dimensionless film thickness.

$$\delta^+ = \left(\left(0.34Re_{\mathrm{LF}}^{0.6}\right)^{2.5} + \left(0.0379Re_{\mathrm{LF}}^{0.9}\right)^{2.5}\right)^{0.4} \tag{2.18}$$

They demonstrated a good agreement with experimental data from Sacks [41] for R11 and R22 for liquid fraction and pressure drop. Moreover, solving the turbulent thermal diffusivity by analogy with the momentum diffusivity, they predicted the heat transfer coefficient and compared it against experimental data from Wattelet [42] for R134a and R22, Dobson [43] for R134a and R22 and Sacks [41] for R12, R11 and R22. The comparison for the heat transfer coeffcient resulted to be satisfactory.

Ambrosini [38, 44, 45] recollected the Asali's and Kosky's correlations and found a new expression which best fitted a wide range of experimental data, on varying channel diameters and working fluids.

$$\delta^+ = \begin{cases} 0.34 Re_{\mathrm{LF}}^{0.6}, & \text{if } Re_{\mathrm{LF}} \leq 1000; \\ 0.0512 Re_{\mathrm{LF}}^{-0.875}, & \text{if } Re_{\mathrm{LF}} > 1000. \end{cases} \tag{2.19}$$

Henstock and Hanratty [46] carried out two correlations for the liquid film thickness, one for horizontal flows, reported in Eq. (2.20),

$$\frac{\delta}{D} = \frac{6.59F}{(1+850F)^{0.5}}, \qquad 10^3 < Re_{\mathrm{LF}} < 10^4 \tag{2.20}$$

and Eq. (2.21) for vertical flows.

$$\frac{\delta}{D} = \frac{6.59F}{(1+1400F)^{0.5}}, \qquad 10 < Re_{\mathrm{LF}} < 10^4 \tag{2.21}$$

where

$$F = \frac{1}{2^{0.5} Re_{\mathrm{V}}^{0.4}} \frac{Re_{\mathrm{LF}}^{0.5}}{Re_{\mathrm{V}}^{0.9}} \frac{\rho_{\mathrm{V}}^{0.5}}{\rho_{\mathrm{L}}^{0.5}} \frac{\mu_{\mathrm{L}}}{\mu_{\mathrm{V}}} \tag{2.22}$$

Tatterson et al. [47] proposed a new way to calculate the parameter F to be used in Eqs. (2.20) and (2.21).

$$F = \frac{\left(\left(0.707 Re_{\mathrm{LF}}^{0.5}\right)^{2.5} + \left(0.0379 Re_{\mathrm{LF}}^{0.9}\right)^{2.5}\right)^{0.4}}{Re_{\mathrm{V}}^{0.9}} \left(\frac{\rho_{\mathrm{V}}}{\rho_{\mathrm{L}}}\right)^{0.5} \frac{\mu_{\mathrm{L}}}{\mu_{\mathrm{V}}} \tag{2.23}$$

It should be noted that the vapour Reynolds number, which appears in Eqs. (2.22) and (2.23), it is calculated considering the tube diameter as characteristic length. In Fukano's work [44], two expressions for liquid film thickness prediction in vertical upward flows for air-water was presented. The Hori's correlation is:

$$\frac{\delta}{D} = 0.905 Re_{\mathrm{JV}}^{-1.45} Re_{\mathrm{JL}}^{0.9} Fr_{\mathrm{V}}^{0.93} Fr_{\mathrm{L}}^{-0.68} \left(\frac{\mu_{\mathrm{L}}}{\mu_{\mathrm{L,ref}}}\right)^{0.5} \tag{2.24}$$

where $\mu_{\mathrm{L,ref}}$ refers to the water dynamic viscosity at 20 °C. The Fukano's correlation is given by:

$$\frac{\delta}{D} = 0.0594 \exp\left(-0.34 Fr_{\mathrm{V}}^{-0.25} {Re_{\mathrm{JL}}}^{0.19} \left(\frac{J_{\mathrm{V}}\rho_{\mathrm{V}}}{J_{\mathrm{V}}\rho_{\mathrm{V}} + J_{\mathrm{L}}\rho_{\mathrm{L}}}\right)^{0.6}\right) \tag{2.25}$$

Hori's and Fukano's correlations are valid in the limits of their experimental data. In Eqs. (2.24) and (2.25) the liquid Reynolds number Re_{L} is computed with the whole liquid phase mass flow rate, whereas the liquid and vapour Froude number are calculated as:

$$Fr_{\mathrm{L}} = \frac{J_{\mathrm{L}}}{(gD)^{0.5}} \tag{2.26}$$

$$Fr_{\mathrm{V}} = \frac{J_{\mathrm{V}}}{(gD)^{0.5}} \tag{2.27}$$

Okawa et al. [48] proposed a method to predict the liquid film thickness from a force balance between interfacial shear stress and wall friction acting on the liquid film:

$$\delta = \frac{1}{4}\left(\frac{f_{\mathrm{W}}\rho_{\mathrm{L}}}{f_{\mathrm{i}}\rho_{\mathrm{V}}}\right)^{0.5}\frac{J_{\mathrm{LF}}}{J_{\mathrm{V}}}D \tag{2.28}$$

where f_{W} is the wall friction factor, evaluated with $max(16/Re_{\mathrm{LF}}, 0.005)$, f_{i} is the interfacial friction factor obtained by the Wallis' correlation.

Finally, it is worth mentioning a correlation for bottom film thickness in horizontal annular flow. The first author was Spurret [49] to propose such a correlation. This was later modified by Roberts et al. [49], according to the Jepson's assumption [49] that the ratio δ/D at the tube bottom is constant under the same superfical velocities. The Robert's correlation is given below.

$$\delta^{+} = 846\frac{D}{D_{\mathrm{ref}}}\frac{Re_{\mathrm{LF}}^{0.44}}{Re_{\mathrm{V}}^{0.59}} \tag{2.29}$$

where D_{ref} is a reference diameter and is equal to 0.026 m. The shear stress to be used in Eq. (2.29) is a wall shear stress for vapour single-phase flow proposed by Asali [39].

2.1.3 Correlations for the liquid film distribution

Recently, some authors attempted to proposed correlations for the liquid film distribution. Hurlburt and Newell [31] introduced a correlation to calculate the ratio between average film thickness and bottom film thickness. It is give by the following:

$$\delta_{\mathrm{a}}\delta_{\mathrm{b}}^{-1} = 0.2 + 0.7\left(1 - \exp\left(-\frac{(x/(1-x))^{0.5}(J_V)/(gD)^{0.5} - 20}{75}\right)\right) \tag{2.30}$$

Schubring and Shedd [50] proposed the following correlation for the ratio between top film thickness and bottom film thickness:

$$\delta_{\mathrm{t}}\delta_{\mathrm{b}}^{-1} = 1 - \exp\left(-0.63\frac{xG}{\rho_{\mathrm{L}}(g\delta_{\mathrm{a}})^{0.5}}\right) \tag{2.31}$$

Cioncolini and Thome [51] recommended the following correlations, validated against a wide experimental database for air-water:

$$\delta_{\mathrm{t}}\delta_{\mathrm{b}}^{-1} = \frac{0.0789Fr^{1.9}}{1 + 0.0789Fr^{1.9}} \tag{2.32}$$

$$\delta_{\mathrm{a}}\delta_{\mathrm{b}}^{-1} = \frac{0.366Fr^{1.45}}{1 + 0.366Fr^{1.45}} \tag{2.33}$$

where the Froude number Fr has to be computed as

$$Fr = \frac{xG}{\rho_{\mathrm{V}}(\rho_{\mathrm{L}} - \rho_{\mathrm{V}})gD} \tag{2.34}$$

A correlation for the entire liquid film distribution has been proposed by Mauro et al. [52]. Using Eqs. (2.32) and (2.33) by Cioncolini and Thome [51] to calculate the film thickness at the tube top and bottom, the distribution is given by the following:

$$\delta(\theta)=\begin{cases} R-\dfrac{2\left(R-\delta_{\mathrm{a}}\right)^{2}\left(R-\delta_{\mathrm{t}}\right)}{\left(2R-\delta_{\mathrm{t}}-\delta_{\mathrm{b}}\right)\left(\left(\frac{2\left(R-\delta_{\mathrm{a}}\right)^{2}}{2R-\delta_{\mathrm{t}}-\delta_{\mathrm{b}}}\cos\theta\right)^{2}+\left(\left(R-\delta_{\mathrm{t}}\right)\sin\theta\right)^{2}\right)^{0.5}}, & \text{if } 0\leq\theta\leq\pi/2; \\ R-\dfrac{2\left(R-\delta_{\mathrm{a}}\right)^{2}\left(R-\delta_{\mathrm{b}}\right)}{\left(2R-\delta_{\mathrm{t}}-\delta_{\mathrm{b}}\right)\left(\left(\frac{2\left(R-\delta_{\mathrm{a}}\right)^{2}}{2R-\delta_{\mathrm{t}}-\delta_{\mathrm{b}}}\cos\theta\right)^{2}+\left(\left(R-\delta_{\mathrm{b}}\right)\sin\theta\right)^{2}\right)^{0.5}}, & \text{if } \pi/2\leq\theta\leq\pi; \end{cases} \tag{2.35}$$

2.2 Prediction of the interfacial shear stress

In annular flow, the liquid film tends to behave as a rough wall on the vapour core [21, 53]. According to the fluid dynamics theory of single-phase flow, the interfacial shear stress is defined as [21, 20]:

$$\tau_{\mathrm{i}}=\frac{1}{2}f_{\mathrm{i}}\rho_{\mathrm{V}}\left(u_{\mathrm{V}}-u_{\mathrm{i}}\right)^{2} \tag{2.36}$$

where f_{i} and u_{i} are the interfacial friction factor and the interfacial velocity, respectively. It is worth noting that, in order to calculate the interfacial shear stress, equations or correlations are needed for the interfacial friction factor and the interfacial velocity. Most authors neglect the interface velocity, assuming that it is small compared to the vapour velocity. This is a reliable assumption for gas-liquid or water-steam flows at near-ambient pressure, because of high values assumed by the ratio between liquid phase density and vapour phase density. For low values of density ratio, as instance in refrigerants flow, this assumption may not be valid.

2.2.1 Interfacial shear stress correlations

The first author to propose a correlation for the interfacial shear stress was Wallis [21]. The correlation for the friction factor is:

$$f_{\mathrm{i}}=0.005\left(1+300\frac{\delta}{D}\right) \tag{2.37}$$

Wallis noted a very interesting similarity to the Nikuradse's relationship for the sand-grain roughness friction factor. Being k_{s} the sand-grain roughness height, he found that $k_{\mathrm{s}}=4\delta$ [53]. To better fit experimental data, the Wallis' correlation was later modified in the following.

$$f_{\mathrm{i}}=f_{\mathrm{V}}\left(1+300\frac{\delta}{D}\right) \tag{2.38}$$

where f_{V} is the single-phase vapour friction factor. Wallis proposed to estimate the interfacial velocity as [21, 20]:

$$u_{\mathrm{i}} = 2u_{\mathrm{L}} \tag{2.39}$$

All the interfacial friction factor correlations are essentially functions of the vapour Reynolds number and the ratio δ/D. For sake of uniformity, the vapour Reynolds number is calculated with the vapour core hydraulic diamater as characteristic length, even on the assumption that $\delta << D$. It is undoubtedly that the Wallis' correlation is the most used. However, as pointed out by Fore et al. [53], it may not be accurate at fully rough regimes, namely regimes in which the friction factor is independent of the vapour Reynolds number, or at transition roughness regimes, which are regimes at low values of vapour Reynolds numer and large ratio δ/D.

Moeck [54] suggested a correlation for annular flows in disturbance wave regimes:

$$f_{\mathrm{i}} = 0.005\left(1 + 1458\left(\frac{\delta}{D}\right)^{1.42}\right) \tag{2.40}$$

Henstock and Hanratty [46], to best fit several experimental data, proposed the following implicit correlation:

$$f_{\mathrm{i}} = f_{\mathrm{V}}\left(1 + 212\left(\frac{f_{\mathrm{i}}}{f_{\mathrm{V}}}\right)^{0.5}\frac{\delta}{D}\right) \tag{2.41}$$

In the study of Fukano and Furukawa [44], the Hori's correlation, reported in Eq. (2.42), was validated against their experimental data for air-water and air-aqueous glycerol solution vertical annular flow, with channel diameter of 26.0 mm and 19.2 mm.

$$f_{\mathrm{i}} = 0.2825\left(Re_{\mathrm{JV}}^{-0.89}Re_{\mathrm{JL}}^{0.68}Fr_{\mathrm{V}}^{0.25}Fr_{\mathrm{L}}^{-0.45}\left(\frac{\mu_{\mathrm{L}}}{\mu_{\mathrm{w,ref}}}\right)^{0.77}\right) \tag{2.42}$$

A satisfactory agreement was only found for large values of Re_{VO}. Fukano and Furukawa [44] compared their experimental data with other two correlations as well, reported in Eqs. (2.43) (for horizontal rectangular ducts) and (2.44) (for vertical channels), respectively.

$$f_{\mathrm{i}} = f_{\mathrm{V}}\left(1 + 6.1\cdot 10^{-5}\chi^{0.52}\left(\frac{\dot{V}_{\mathrm{L}}'}{\upsilon_{\mathrm{L}}}\right)^{0.65}Re_{\mathrm{JV}}^{0.7}\right) \tag{2.43}$$

$$f_{\mathrm{i}} = 0.425\left(12 + \frac{\upsilon_{\mathrm{L}}}{\upsilon_{\mathrm{w,ref}}}\right)^{-1.33}\left(1 + 12\frac{\delta}{D}\right)^{8} \tag{2.44}$$

where $\dot{V}_{\mathrm{L}}'$ is the liquid volumetric flow rate per unit width and $\upsilon_{\mathrm{w,ref}}$ is the kinematic viscosity of liquid water at 20 °C.

whereas Eq. (2.43) showed satisfactory agreement only for $Re_{\mathrm{VO}} > 5\cdot 10^{4}$, Eq. (2.44) resulted to be a good predictor in the whole range of their experimental data. The reason for this behaviour is indeed an important remark: for vertical annular flows, the liquid film thickness is mainly controlled by the gravity force at low values of vapour Reynolds number; in horizontal annular flows the average value of the liquid film thickness is controlled by the interfacial shear stress instead.

Another implict correlation was found by Asali et al. [39]:

$$f_{\mathrm{i}} = f_{\mathrm{V}} \left(1 + 0.45 Re_{\mathrm{V}}^{-0.2} \left(Re_{\mathrm{V}} \left(\frac{f_{\mathrm{i}}}{2} \right)^{0.5} \frac{\delta}{D} - 4 \right) \right) \tag{2.45}$$

In order to better predict the interfacial friction factor at transition roughness regimes, Fore et al. [53] proposed the following adaptation of Wallis' correlation:

$$f_{\mathrm{i}} = 0.005 \left(1 + 300 \left(\left(1 + \frac{17500}{Re_{\mathrm{V}}} \right) \frac{\delta}{D} - 0.0015 \right) \right) \tag{2.46}$$

Eq. (2.46) was validated against experimental data from Asali [55], Fore and Dukler [56, 57], and Fore et al. [53], for several gas-liquid flow, in a range of channel diameter between 9.68 mm and 50.8 mm, pressure up to 17 atm, temperature between 17 °C and 93 °C. The agreement resulted to be satisfactory.

Ashwood et al. [58] recommended to use a correlation which is dependent on the intermittency of the disturbance waves. The expression is:

$$f_{\mathrm{i}} = \left(0.079 Re_{\mathrm{V}}^{-0.25} \right) \left(1 + 18.7 Re_{\mathrm{V}}^{-0.5} \left(\frac{\mu_{\mathrm{L}}}{\mu_{\mathrm{V}}} \left(\frac{\rho_{\mathrm{V}}}{\rho_{\mathrm{L}}} \right)^{0.5} \delta^{+} (1 + INT) \right) \right) \tag{2.47}$$

where the disturbance wave intermittency INT has to be calculated by means of the following:

$$INT = 0.1 + \frac{Re_{\mathrm{L}}}{4 \cdot 10^{4}} \tag{2.48}$$

A satisfactory agreement was found against experimental data on pressure drop for air-water flows.

Schubring and Shedd [50] and Shedd [32], in order to predict the average liquid film thickness in air-water horizontal flows, used both the Haaland and Colebrook's fully rough correlation:

$$\begin{aligned} (4 f_{\mathrm{i}})^{-0.5} &= -1.8 \log_{10} \left(\frac{6.9}{Re_{\mathrm{core}}} + \left(\frac{RR}{3.7} \right)^{\frac{10}{9}} \right) \\ Re_{\mathrm{core}} &= \frac{\rho_{\mathrm{V}} (u_{\mathrm{V}} - u_{\mathrm{L}})(D - 2\delta)}{\mu_{\mathrm{V}}} \\ RR &= \frac{1}{3} \frac{\delta}{D - 2\delta} x^{0.25} \end{aligned} \tag{2.49}$$

and a modified McAdams' smooth tube correlation:

$$f_{\mathrm{i}} = 0.046\phi_{\mathrm{RR}} Re_{\mathrm{core}}^{-0.2} \tag{2.50}$$

where RR is the relative roughness. In Eq. (2.50), ϕ_{RR} is a correction factor to take the interfacial roughness into account. Best fitting their data, ϕ_{RR} was found to be equal to 1.289. They used both Eqs. (2.49) and (2.50), which determined no significant difference in the results. Their data was reported in Schubring and Shedd [59], resulting in a channel diameter range of 8.8 - 26.3 mm, mass flux range of 71 - 430 $kg/(m^2 s)$, vapour quality range of 0.0119 - 0.782, for air-water flow at near-ambient pressure, founding a good agreement.

Another expression, which uses the relative roughness at the liquid-vapour interface, was proposed by Hurlburt et al. [60] and used by Schubring and Shedd [61] in a model for the prediction of the liquid film thickness and pressure drop:

$$\begin{aligned} f_{\mathrm{i}} &= 0.58^2\left(-\frac{\ln(RR)}{(RR-1)^2} - \ln(0.8) + 1.05 + \frac{1}{2}\frac{RR+1}{RR-1}\right)^{-2} \\ RR &= \frac{4(1-LF)\delta}{D-2\delta} \end{aligned} \tag{2.51}$$

where the laminar fraction LF was declared to be equal to 0.7. In the same work, Schubring and Shedd [61] declared that the model predictions was not sensitive whether a modified Blasius' correlation was used instead of Eq. (2.51):

$$\begin{aligned} f_{\mathrm{i}} &= 0.079\phi_{\mathrm{RR}} Re_{\mathrm{core}}^{-0.25} \\ \phi_{\mathrm{RR}} &= 1.9x^{0.1} \end{aligned} \tag{2.52}$$

where Re_{core} is computed in same way as in Eq. (2.49). Eq. (2.51) was validated against experimental data for gas-liquid horizontal flows from Schubring and Shedd [59], Laurinat [62] and Paras and Karabelas [63], resulting in a good agreement.

2.3 Heat transfer in turbulent liquid film

For a Newtonian fluid in laminar flow, the following relationship between shear stress and velocity gradient is valid:

$$\tau = \mu\frac{\mathrm{d}u}{\mathrm{d}y} \tag{2.53}$$

In turbulent flow, the momentum transport is increased because of the eddy diffusivity ϵ, according to Eq. (2.54):

$$\tau = (\mu + \rho\epsilon)\frac{\mathrm{d}u}{\mathrm{d}y} \tag{2.54}$$

It is possible to define a dimensionless diffusivity ϵ^+ using Eqs. (2.2) and (2.3):

$$\epsilon^+ = \frac{\rho\epsilon}{\mu} \tag{2.55}$$

$$\epsilon^+ = \left(\frac{\mathrm{d}u^+}{\mathrm{d}y^+}\right)^{-1} - 1 \tag{2.56}$$

Using the three-part universal velocity profile, the values of the dimensionless eddy diffusivity can be found as follows:

$$\epsilon^+ = \begin{cases} \text{laminar sublayer:} & 0, & \text{for } y^+ < 5; \\ \text{buffer layer:} & \dfrac{y^+}{5} - 1, & \text{for } 5 < y^+ < 30; \\ \text{turbulent core:} & \dfrac{y^+}{2.5} - 1, & \text{for } y^+ > 30. \end{cases} \tag{2.57}$$

In the same way done for the momentum transport, the thermal energy transport is enhanced by the turbulence. In laminar flow, the heat transfer is transported by the molecular conduction only:

$$\dot{q} = -k\frac{\mathrm{d}T}{\mathrm{d}y} \tag{2.58}$$

In order to quantify the increase in the heat transfer due to the turbulence, the eddy thermal diffusivity ϵ_t is introduced in Eq. (2.59).

$$\dot{q} = -(k + \rho\epsilon_\mathrm{t} c_\mathrm{p})\frac{\mathrm{d}T}{\mathrm{d}y} \tag{2.59}$$

According to the Reynolds analogy, the thermal eddy diffusivity equals the momentum eddy diffusivity. It is convenient to define a dimensionless temperature T^+ as:

$$T^+ = c_\mathrm{p}\frac{(\tau\rho)^{\frac{1}{2}}}{h} \tag{2.60}$$

where h is the heat transfer coeffcient. Using Eqs. (2.3), (2.59) and (2.60), it is possible to obtain the following relationship between dimensionless temperature gradient and dimensionless diffusivity:

$$\frac{\mathrm{d}T^+}{\mathrm{d}y^+} = \frac{1}{1/Pr + \epsilon^+} \tag{2.61}$$

where Pr is the Prandtl number. With Eq. (2.62), the integration of Eq. (2.60) lead to:

$$T^+ = \begin{cases} \text{laminar sublayer: } y^+ Pr, & \text{for } y^+ < 5; \\ \text{buffer layer: } 5\left(Pr + \ln\left(1 + Pr\left(y^+/5 - 1\right)\right)\right), & \text{for } 5 < y^+ < 30; \\ \text{turbulent core: } 2.5\ln\left(\dfrac{y^+ + 2.5(1/Pr - 1)}{30 + 2.5(1/Pr - 1)}\right) + 5(Pr + \ln(1 + 5Pr)), & \text{for } y^+ > 30. \end{cases} \tag{2.62}$$

In conventional channels, the dimensionless liquid film thickness is usually greater than 30, therefore the liquid film assumes a turbulent behaviour. In this case, it is possible to define a thermal resistance for laminar sublayer, buffer layer and turbulent core, respectively, as follows:

$$R_{\mathrm{t}} = \begin{cases} \text{laminar sublayer:} & \dfrac{5Pr}{c_{\mathrm{p}}(\tau\rho)^{\frac{1}{2}}}; \\ \text{buffer layer:} & \dfrac{5\ln(1+5Pr)}{c_{\mathrm{p}}(\tau\rho)^{\frac{1}{2}}}; \\ \text{turbulent core:} & \dfrac{2.5\ln\left(\dfrac{y^{+}+2.5(1/Pr-1)}{30+2.5(1/Pr-1)}\right)}{c_{\mathrm{p}}(\tau\rho)^{\frac{1}{2}}}. \end{cases} \tag{2.63}$$

Cioncolini and Thome [64] proposed a new equation for the dimensionless temperature T^{+} for evaporating annular flow. The latter has been validated against heat transfer coefficient experimental data for water and refrigerants.

2.4 Theoretical and semi-theoretical models

Theoretical and semi-theoretical models, based on one-dimensional mass and momentum equations on the liquid phase, have been proposed by many authors. Okawa et al. [65, 66] performed a one-dimensional mass balance on the liquid film, taking deposition and entrainment rates into account, in order to predict the critical heat flux. Kishore and Jayanti [67] solved three-dimensional mass and momentum equations for the vapour core, whereas the *triangular relationship* and a sand-grain roughness approach for the interfacial shear stress was used for the liquid film flow. Alipchenkov et al. [68] carried out a one-dimensional three-fluid model for annular flow. In such a model, the mass and momentum equations have been applied to the liquid film, gas core and entrained liquid droplets.

A one-dimensional annular flow model was developed by Revellin and Thome [69] in order to predict CHF. They used mass and momentum equations on the liquid phase and the vapour phase to calculate the liquid film thickness and to compare it against a correlation for the interfacial waves. Cioncolini et al. [70] developed a unfied macro-to-micro scale method in order to predict the pressure drop in annular flow. Whan Na and Chung [71] proposed a one-dimensional annular flow model for evaporative heat transfer in microchannels taking the Marangoni effect, the capillarity and the wettability into account.

Cioncolini et al. [35] and Cioncolini and Thome [64] studied the turbulence modelling in annular flow liquid film in anon-adiabatic and in non-adiabatic and evaporating conditions, respectively, assuming a symmetric liquid film distribution. Schubring and Shedd [61] also proposed a one-dimensional model for the pressure drop, film thickness and entrainment fraction predictions considering the intermittency of the disturbance waves. Mass transportation equation was used to determine the entrainment rate by Liu et al. [72] in a VOF scheme in order to model the roll wave flow.

Kim and Mudawar [73, 74] developed two one-dimensional models for condensing and boiling annular flow for microchannels, respectively, in order to predict pressure drop and heat transfer coefficient. In both their studies, mass and momentum equations were applied on each phase, taking the liquid radial velocity profile and a turbulence model into account, although the circumferential gradient was neglected.

Li and Anglart [75] developed a CFD model for evaporating liquid film using a Eulerian-Langrangian approach. The radial and tangential gradients of velocities and pressures was neglected and the entrained droplets was taken into account. Zhang et al. [76] used mas and momentum equations on each phase into a probability model for the prediction of droplet entrainment. Jesseela and Sobhan [77] studied a quasi three dimensional numerical model to analyse flow with phase change in a rectangular microchannel. Their model is found to be capable of obtaining the velocity distribution, two phase pressure drop, an average two phase heat transfer coefficient and the wall temperature corresponding to the annular flow domain in the channel.

The studies cited so far are able to predict the average liquid film thickness in the cross-section, for a given condition. However, it is well-known that the annular flow presents liquid film stratification in horizontal channels, since the gravity force becomes important in specific conditions. Williams [78] introduced a symmetry parameter in order to quantify such a stratification. Laurinat et al. [79] proposed a liquid film thickness model using both mass and momentum equations, although this was accomplished with the aid of a correction factor for a better agreement with experimental data. Fukano and Ousaka [80] modified Laurinat's model in order to include the effect of disturbance waves on the liquid surface. Hurlburt and Newell [31] also developed mass and momentum equations in three coordinates, although they considered a static tangential momentum equation for the liquid phase and ignored any surface tension effect.

Wang and Rose [81] applied mass and momentum equations on the liquid phase in order to predict the liquid film distribution for condensing flow in microchannels. Nebuloni and Thome [82] developed a numerical model for condensing laminar annular flow in microchannels for different channel shapes. Their study contemplates several interface phenomena, such as capillarity, wettability and molecular transport, but they used an one-dimensional equations for the vapour phase. Da Riva et al. [83] used the Volume of Fuid (VOF) method to the annular flow with the purpose to predict liquid film thickness distribution and heat transfer coefficient. Nevertheless, the VOF method requires a considerable computational effort and it has not been validated in a wide range of channel sizes and working fluids.

It is clear that the theoretical modelling of two-phase annular flow is a highly investigated topic of research. However, despite the great number of studies which take many physical phenomena into account, such as radial velocity profile in the liquid film, turbulent flow, wettability effect, there is a lack of theoretical models which solve the mass and momentum equations on both phases and, therefore, able to predict liquid film, interfacial shear stress and field of velocity in the tangential direction with a reasonable computational effort.

2.5 Upward liquid transport mechanisms

As it is well-known, the gravitational force causes the stratification of the liquid film in horizontal annular flow. Nevertheless, it is still not clear which force or transport mechism toward the tube top may sustain the liquid film and, therefore, counterbalance the gravitational liquid transport toward the tube top. The following mechanisms are usually recognised:

- surface tension: in small-diameter channels, the distribution of the interface curvature induces pressure gradient in the tangential direction, pumping the liquid film upward.
- secondary flow (Laurinat et al. [79], Lin et al. [84], Flores et al. [85]): in the cross-section of the channel, counter-rotating velocitiy fields in the vapour phase drag the liquid film upward by tangential shear-stress; secondary flows can be induced by wall-roughness variation (Darling and McManus [86]), by non-uniform droplet concentration (Belt et al. [87]), or by non-circular cross-section (Speziale [88]);
- liquid entrainment and deposition (Russel and Lamb [89]): the entrainment rate is greater at the tube bottom because of the thinner liquid film, whereas the deposition rate may be predominant at the tube top, contributing to replenish the liquid film in the latter zone;
- wave spreading and mixing mechanism (Butterworth and Pulling [90], Jayanti et al. [91]): due to the non-uniform liquid film thickness, the disturbance waves spread over the circumference;
- pumping action of disturbance wave (Fukano and Ousaka [80], Sutharshan et al. [92]).

Sutharshan et al. [92], by means of photo-chromic spot activation technique, demonstrated that the pumping action of the disturbance waves plays the most important role in the liquid upward transport. They showed that the liquid film between two consecutive disturbance waves is continuously drained downward by the gravity. The replenishment of the liquid film at the tube top occurred at the passage of such disturbance waves. Jayanti and Hewitt [93], by means of CFD simulations, showed that the secondary flows are induced by the tangential variation of the interfacial roughness. Nevertheless, an axial variation of such interfacial roughness destroys the secondary flows near the interface, negating the possibility to redistribute the liquid film along the tube circumference by such a mechanism.

Recently, Fukano and Inatomi [94], carrying out a Direct Navier-Stokes (DNS) analysis for horizontal annular flow, stated that the predominant mechanism is the pumping action of disturbance waves. van't Westende et al. [95] investigated the role of the secondary flows on the deposition rate of liquid droplets. They stated the secondary flows may ensure a near-uniform deposition rate over the circumference, contrasting the effect of the gravitational force on the liquid droplets.

McCaslin and Desjardins [96] analysed the gravitational effect on horizontal gas-liquid annular flow, showing that ripples and deposition are mostly responsible to the transport of the liquid phase upward and to supply the top film thickness.

Chapter 3

A TWO-DIMENSIONAL MODEL FOR ANNULAR FLOW

In this study, a new model for horizontal two-phase annular flow in circular channels is presented. Two-dimensional mass and momentum equations are applied on the liquid and the vapour phases, neglecting the variation along the radial direction of velocity and pressure. Nevertheless, laminar or turbulent conditions are taken into consideration. The capillarity is solely contemplated as interface phenomenon. The scope of the model is to reduce the number of equations and, hence, the computational time with respect to the most detailed models currently available in literature. In spite of the reduction of equations, a validation based on experimental data over a wide range of operational conditions for pressure drops and liquid film thickness is presented. The range of operational conditions in terms of reduced pressure, channel diameter and working fluid is the wider available in literature, including those conditions affected by intense stratification.

3.1 Derivation of the fundamental equations

The main feature to be performed by the model is the liquid film distribution along the wall of the pipe. It is well-known that such distribution is solely caused by the gravity, if any other mass forces on the liquid phase are not involved. A semi-theoretical two-dimensional model for two-phase annular flow is derived afterwards. Such a model is derived from the fundamental equations of mass conservation and momentum balance. The assumptions on which the equations are based are:

- annular flow pattern;
- steady state flow;
- in non-anon-adiabatic condition, the thermal power is entirely used for the phase

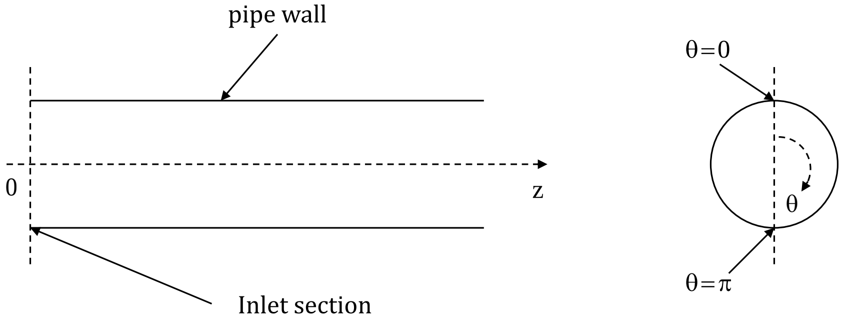

Figure 3.1: Reference system in cylindrical coordinates.

change, in such a way that the following energy balance is verified:

$$\mathrm{d}\dot{m}_{\mathrm{LV}} = \frac{\dot{q} \cdot \mathrm{d}A_{\mathrm{ht}}}{h_{\mathrm{LV}}} \tag{3.1}$$

where $\mathrm{d}\dot{m}_{\mathrm{LV}}$ is the mass flow rate of phase change in a elementary control volume, $\dot{q}$ is the heat flux at the wall, $\mathrm{d}A_{\mathrm{ht}}$ is the elementary heat transfer area and h_{LV} is the latent heat of vaporization.

- smooth liquid-vapour interface;
- no entrainment of liquid droplets in the vapour core.

3.1.1 Coordinate reference system

A cylindrical coordinates system is used as illustrated in Fig. 3.1. The height axis z lies in the axis of symmetry of the pipe, on the flow's direction, and the point $z = 0$ is set to the inlet section. The azimuthal axis θ is located along the tangential direction of the channel section and points downward. For sake of reference, in each section the points at $\theta = 0$ and $\theta = \pi$ are referred as tube top and tube bottom, respectively.

3.1.2 Description of the geometry

Because of the assumption of annular flow, the vapour phase flows as a core enclosed by a liquid film which wets the entire periphery of the wall. Referring to the cylindrical coordinates, the liquid-vapour interface is completely described by the radius of the vapour core $r(z,\theta)$. Taking into consideration an infinitesimal control volume, the view sections are shown in Fig. 3.2, for the axial direction and for the tangential direction respectively. For the definition of the surfaces of interest, two subscripts are used: the first indicates the phase, the second designates the normal direction to the surface.

$$A_{\mathrm{L,z}} = \frac{R^2 - r^2}{2} \mathrm{d}\theta \tag{3.2}$$

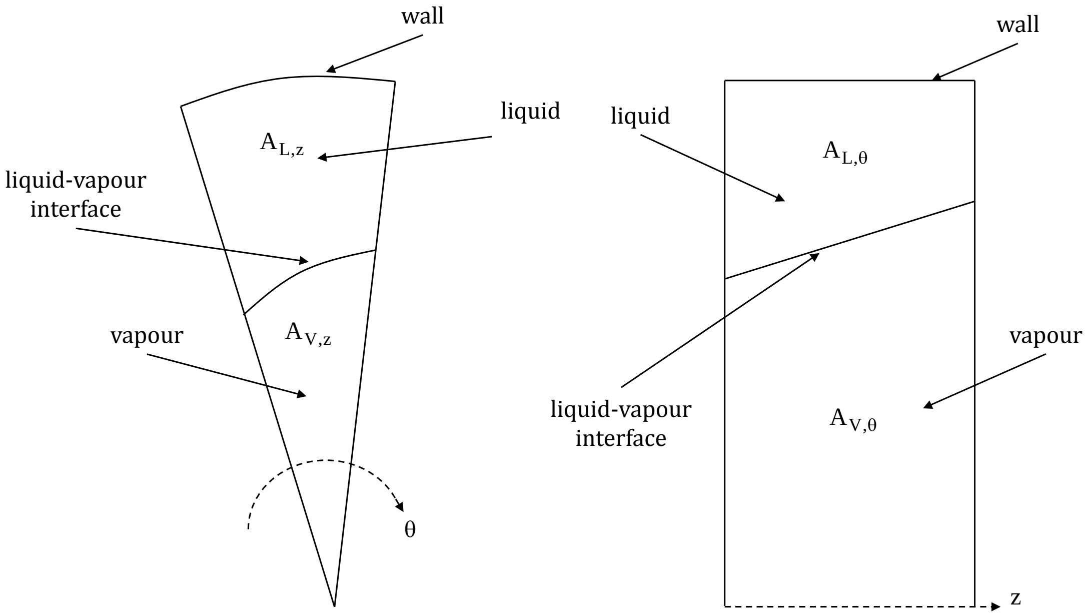

Figure 3.2: Views sections of an infinitesimal control volume.

$$A_{\mathrm{V,z}} = \frac{r^2}{2} \mathrm{d}\theta \tag{3.3}$$

$$A_{\mathrm{L,\theta}} = (R - r)\,\mathrm{d}z \tag{3.4}$$

$$A_{\mathrm{V,\theta}} = r\mathrm{d}z \tag{3.5}$$

For the infinitesimal area of the liquid-vapour interface the subscript i is used, whereas LW indicates the contact surface between the liquid film and the tube wall.

$$A_{\mathrm{i}} = r\mathrm{d}z\mathrm{d}\theta \tag{3.6}$$

$$A_{\mathrm{LW}} = R\mathrm{d}z\mathrm{d}\theta \tag{3.7}$$

It is worth mentioning that the liquid-wall contact surface A_{LW} equals the elementary heat transfer area $\mathrm{d}A_{\mathrm{ht}}$.

3.1.3 Liquid-vapour interface equation

In two-phase flow, the liquid-vapour interfase can be modelled as an infinitely thin membrane having a stretching resistance, which is quantified by the surface tension σ. The Young-Laplace equation states that the difference between the vapour pressure and the liquid pressure is a function of the surface tension and the mean curvature of the interface:

$$p_{\mathrm{V}} - p_{\mathrm{L}} = 2\sigma\kappa \tag{3.8}$$

The mean curvature κ is a geometrical property of a surface [97], and it is defined as follows:

$$\kappa = \frac{1}{\gamma_1} + \frac{1}{\gamma_2} \tag{3.9}$$

In Eq. (3.9), γ_1 and γ_2 are the principal radii of curvature. Accordingly to the geometry of the annular flow pattern, the radius of curvature in the axial direction is significantly larger than the one in the tangential direction. Hence, the mean curvature is computed considering only the dependence of r along the θ axis. In polar coordinates, the curvature is determined as:

$$\kappa = \frac{r^2 + \left(\frac{\partial r}{\partial \theta}\right)^2 - r\left(\frac{\partial^2 r}{\partial \theta^2}\right)}{\left(r^2 + \left(\frac{\partial r}{\partial \theta}\right)^2\right)^{\frac{3}{2}}} \tag{3.10}$$

3.1.4 Mass balance for the liquid phase

The mass variation in the liquid phase is due to the phase change, as illustrated in Fig. 3.3. As a vector quantity, the velocity can be decomposed in the two scalar quantities u and v, which indicate the velocity of each phase in the axial direction and in the tangential direction, respectively. The liquid mass balance in a infinitesimal control volume is given by the Eq. (3.11).

$$\mathrm{d}\dot{m}_{\mathrm{L,z}} + \mathrm{d}\dot{m}_{\mathrm{L,\theta}} = -\mathrm{d}\dot{m}_{\mathrm{LV}} \tag{3.11}$$

Rearranging the Eq. (3.11) with the definition of the surfaces in Eqs. (3.2) and (3.4) and the energy balance in Eq. (3.1), the liquid mass balance leads to Eq. (3.12) and Eq. (3.13).

$$\frac{\partial\left(A_{\mathrm{L,z}} u_{\mathrm{L}}\right)}{\partial z}\mathrm{d}z + \frac{\partial\left(A_{\mathrm{L,\theta}} v_{\mathrm{L}}\right)}{r\partial\theta} r\mathrm{d}\theta = -\frac{\dot{q}\cdot R}{\rho_{\mathrm{L}} h_{\mathrm{LV}}}\mathrm{d}z\mathrm{d}\theta \tag{3.12}$$

$$-u_{\mathrm{L}} r\frac{\partial r}{\partial z} + \frac{R^2 - r^2}{2}\frac{\partial u_{\mathrm{L}}}{\partial z} - v_{\mathrm{L}}\frac{\partial r}{\partial \theta} + (R-r)\frac{\partial v_{\mathrm{L}}}{\partial \theta} = -\frac{\dot{q}\cdot R}{\rho_{\mathrm{L}} h_{\mathrm{LV}}} \tag{3.13}$$

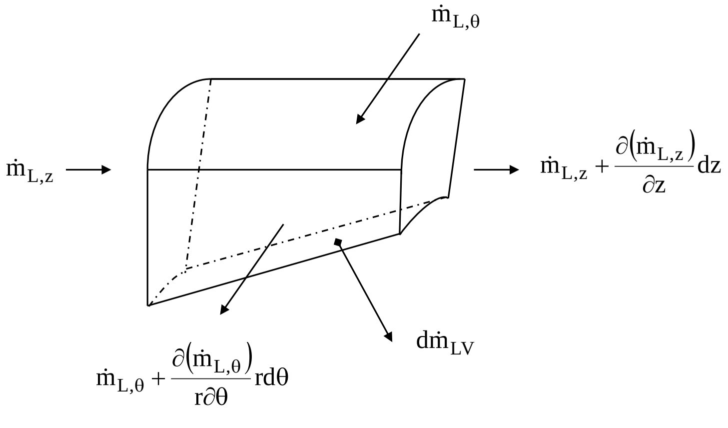

Figure 3.3: Mass balance on an infinitesimal control volume for the liquid phase.

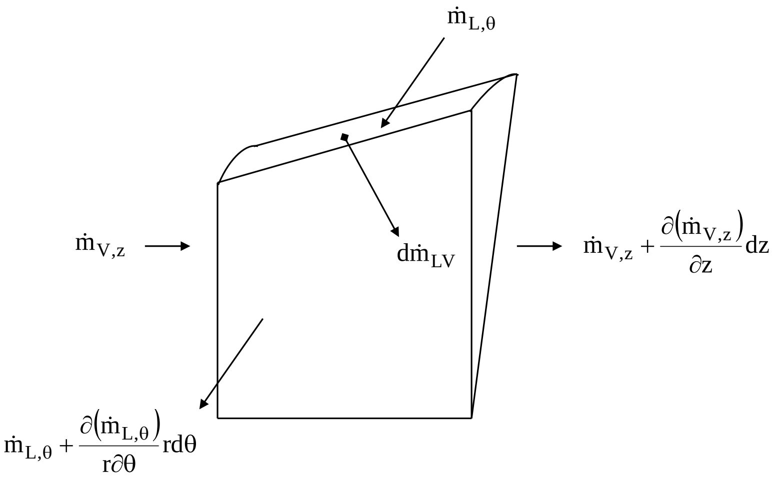

Figure 3.4: Mass balance on an infinitesimal control volume for the vapour phase.

3.1.5 Mass balance for the vapour phase

As shown in Fig. 3.4, the mass balance for the vapour phase can be formulated as in Eq. (3.14). It should be noted that the choice of sign in the source term is congruent with an evaporation process. However, the mass balance equations are still valid for a condensing flow if a negative heat flux is considered.

$$d\dot{m}_{V,z} + d\dot{m}_{V,\theta} = d\dot{m}_{LV} \tag{3.14}$$

Using Eqs. (3.3) and (3.5) for the surfaces and the energy balance in Eq. (3.1), the vapour mass balance can be arranged as follows:

$$\frac{\partial\left(A_{V,z}u_V\right)}{\partial z}dz + \frac{\partial\left(A_{V,\theta}v_V\right)}{r\partial\theta}rd\theta = \frac{\dot{q}\cdot R}{\rho_V h_{LV}}dzd\theta \tag{3.15}$$

$$u_V r\frac{\partial r}{\partial z} + \frac{r^2}{2}\frac{\partial u_V}{\partial z} + v_V\frac{\partial r}{\partial\theta} + r\frac{\partial v_V}{\partial\theta} = \frac{\dot{q}\cdot R}{\rho_V h_{LV}} \tag{3.16}$$

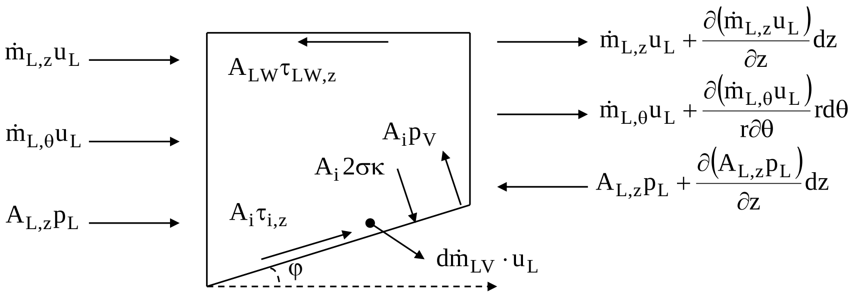

Figure 3.5: Momentum balance in the axial direction for the liquid phase.

3.1.6 Momentum equation in the axial direction for the liquid phase

For an infinitesimal control volume on the liquid phase, the momentum equation along the z direction is shown graphically in Fig. 3.5. It should be noted that an angle ϕ is needed because of the inclination of the liquid-vapour interface. Two frictional shear stresses appear at the wall surface and at the liquid-vapour interface, respectively. The latter points the flow's direction, because, in such situations, the relation $u_\mathrm{V} > u_\mathrm{L}$ is verified. Finally, a source term is present due to the phase change. The z–momentum balance for the liquid phase assumes, hence, the form expressed in Eq. (3.17).

$$\rho_\mathrm{L} \frac{\partial \left(A_\mathrm{L,z} u_\mathrm{L}^2\right)}{\partial z} \mathrm{d}z + \rho_\mathrm{L} \frac{\partial \left(A_{\mathrm{L},\theta} v_\mathrm{L} u_\mathrm{L}\right)}{r\partial\theta} r\mathrm{d}\theta = -\frac{\partial \left(A_\mathrm{L,z} p_\mathrm{L}\right)}{\partial z}\mathrm{d}z + \\ A_\mathrm{i} 2\sigma\kappa \sin(\phi) - A_\mathrm{i} p_\mathrm{V} \sin(\phi) - \mathrm{d}\dot{m}_\mathrm{LV} u_\mathrm{L} + A_\mathrm{i}\tau_\mathrm{i,z} c_\mathrm{z}(\phi) - A_\mathrm{LW}\tau_\mathrm{LW,z} \tag{3.17}$$

$c_\mathrm{z}(\theta)$, defined in Eq. (3.18), is a correction factor which takes into account the inclination of the interface with respect to the z axis.

$$c_\mathrm{z}(\phi) = \cos\left(\arctan\left(\frac{\partial r}{\partial z}\right)\right) \tag{3.18}$$

Using the Eqs. (3.2) and (3.4) for the surfaces, the Young-Laplace equation Eq. (3.8), and Eq. (3.1) for the energy balance, Eq. (3.17) can be rearranged as follows:

$$\rho_\mathrm{L} \frac{\partial \left(A_\mathrm{L,z} u_\mathrm{L}^2\right)}{\partial z} \mathrm{d}z + \rho_\mathrm{L} \frac{\partial \left(A_{\mathrm{L},\theta} v_\mathrm{L} u_\mathrm{L}\right)}{r\partial\theta} r\mathrm{d}\theta = \\ -A_\mathrm{L,z}\frac{\partial p_\mathrm{L}}{\partial z}\mathrm{d}z - \frac{\dot{q}\cdot R}{h_\mathrm{LV}} u_\mathrm{L}\mathrm{d}z\mathrm{d}\theta + A_\mathrm{i}\tau_\mathrm{i,z} c_\mathrm{z}(\phi) - A_\mathrm{LW}\tau_\mathrm{LW,z} \tag{3.19}$$

$$-\rho_\mathrm{L} u_\mathrm{L}^2 r \frac{\partial r}{\partial z} + \rho_\mathrm{L}\left(R^2 - r^2\right) u_\mathrm{L}\frac{\partial u_\mathrm{L}}{\partial z} - \rho_\mathrm{L} v_\mathrm{L} u_\mathrm{L}\frac{\partial r}{\partial \theta} + \rho_\mathrm{L}(R-r) u_\mathrm{L}\frac{\partial v_\mathrm{L}}{\partial\theta} + \rho_\mathrm{L}(R-r) v_\mathrm{L}\frac{\partial u_\mathrm{L}}{\partial\theta} = \\ -\frac{\left(R^2 - r^2\right)}{2}\frac{\partial p_\mathrm{L}}{\partial z} - \frac{\dot{q}\cdot R}{h_\mathrm{LV}} u_\mathrm{L} + r\tau_\mathrm{i,z} c_\mathrm{z}(\phi) - R\tau_\mathrm{LW,z} \tag{3.20}$$

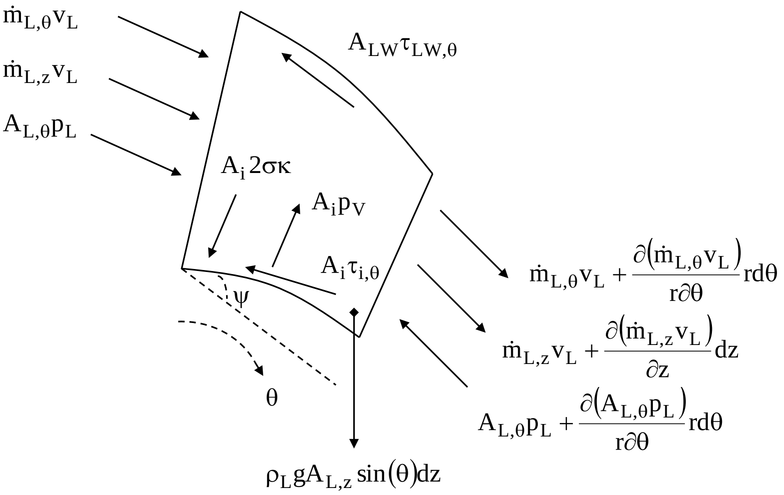

Figure 3.6: Momentum balance in the tangential direction for the liquid phase.

3.1.7 Momentum equation in the tangential direction for the liquid phase

The forces acting on the liquid phase infinitesimal control volume in the tangential direction are shown in Fig. 3.6. A gravitational force appears in the balance. This term is extremely important because it is responsible for the liquid film stratification. An angle ψ is introduced, in order to quantify the inclination of the interface with respect to the θ axis. It is worth noting that the interfacial shear stress is opposed to the flow verse. This occurs because v_L and v_V are opposite in sign. The momentum equation in the tangential direction for the liquid phase is given by the following equation:

$$\begin{aligned}&\rho_{\mathrm{L}}\frac{\partial\left(A_{\mathrm{L},\theta}v_{\mathrm{L}}^2\right)}{r\partial\theta}r\mathrm{d}\theta+\rho_{\mathrm{L}}\frac{\partial\left(A_{\mathrm{L,z}}u_{\mathrm{L}}v_{\mathrm{L}}\right)}{\partial z}\mathrm{dz}=-\frac{\partial\left(A_{\mathrm{L},\theta}p_{\mathrm{L}}\right)}{r\partial\theta}r\mathrm{d}\theta+\\&A_{\mathrm{i}}2\sigma\kappa\sin(\psi)-A_{\mathrm{i}}p_{\mathrm{V}}\sin(\psi)+\rho_{\mathrm{L}}gA_{\mathrm{L,z}}\sin(\theta)\mathrm{dz}-A_{\mathrm{i}}\tau_{\mathrm{i},\theta}c_{\theta}(\psi)-A_{\mathrm{LW}}\tau_{\mathrm{LW},\theta}\end{aligned}\tag{3.21}$$

For the inclination of the liquid-vapour interface, the correction factor $c_\theta(\psi)$ is computed as in Eq. (3.22).

$$c_{\theta}(\psi)=\cos\left(\arctan\left(\frac{\partial r}{r\partial\theta}\right)\right)\tag{3.22}$$

Rearranging Eq. (3.21) with Eqs. (3.2), (3.4) and (3.8), the following can be obtained:

$$\begin{aligned}&\rho_{\mathrm{L}}\frac{\partial\left(A_{\mathrm{L},\theta}v_{\mathrm{L}}^2\right)}{r\partial\theta}r\mathrm{d}\theta+\rho_{\mathrm{L}}\frac{\partial\left(A_{\mathrm{L,z}}u_{\mathrm{L}}v_{\mathrm{L}}\right)}{\partial z}dz=\\&-A_{\mathrm{L},\theta}\frac{\partial p_{\mathrm{L}}}{r\partial\theta}r\mathrm{d}\theta+\rho_{\mathrm{L}}gA_{\mathrm{L,z}}\sin(\theta)\mathrm{dz}-A_{\mathrm{i}}\tau_{\mathrm{i},\theta}c_{\theta}(\psi)-A_{\mathrm{LW}}\tau_{\mathrm{LW},\theta}\end{aligned}\tag{3.23}$$

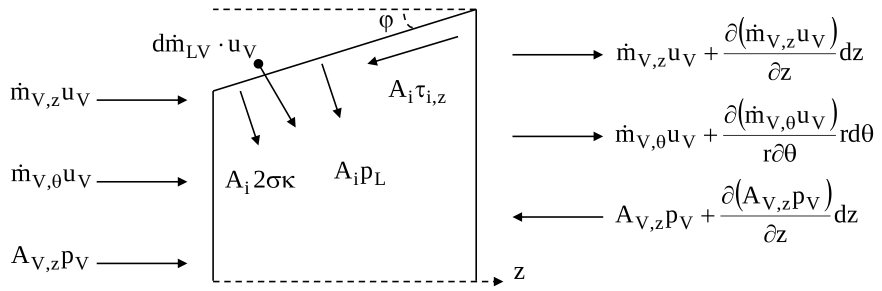

Figure 3.7: Momentum balance in the axial direction for the vapour phase.

$$-\rho_{\mathrm{L}}v_{\mathrm{L}}^2\frac{\partial r}{\partial\theta}+2\rho_{\mathrm{L}}(R-r)v_{\mathrm{L}}\frac{\partial v_{\mathrm{L}}}{\partial\theta}-\rho_{\mathrm{L}}u_{\mathrm{L}}v_{\mathrm{L}}r\frac{\partial r}{\partial z}+\rho_{\mathrm{L}}\frac{\left(R^2-r^2\right)}{2}v_{\mathrm{L}}\frac{\partial u_{\mathrm{L}}}{\partial z}+\rho_{\mathrm{L}}\frac{\left(R^2-r^2\right)}{2}u_{\mathrm{L}}\frac{\partial v_{\mathrm{L}}}{\partial z}=$$

$$-(R-r)\frac{\partial p_{\mathrm{L}}}{\partial\theta}+\rho_{\mathrm{L}}g\frac{\left(R^2-r^2\right)}{2}\sin(\theta)-r\tau_{\mathrm{i,\theta}}c_{\theta}(\psi)-R\tau_{\mathrm{LW,\theta}} \tag{3.24}$$

3.1.8 Momentum equation in the axial direction for the vapour phase

The vapour phase infinitesimal control volume is shown in Fig. 3.7, including the forces acting in the axial direction. The angle ϕ appears in order to quantify the inclination of the interface, as done for the liquid phase. The frictional shear stress at the interface is reverse in respect to the vapour flow. The momentum equation assumes the following expression:

$$\rho_{\mathrm{V}}\frac{\partial\left(A_{\mathrm{V,z}}u_{\mathrm{V}}^2\right)}{\partial z}\mathrm{d}z+\rho_{\mathrm{v}}\frac{\partial\left(A_{\mathrm{V,\theta}}v_{\mathrm{V}}u_{\mathrm{V}}\right)}{r\partial\theta}r\mathrm{d}\theta=-\frac{\partial\left(A_{\mathrm{V,z}}p_{\mathrm{V}}\right)}{\partial z}\mathrm{d}z$$

$$A_{\mathrm{i}}2\sigma\kappa\sin(\phi)+A_{\mathrm{i}}p_{\mathrm{L}}\sin(\phi)+\mathrm{d}\dot{m}_{\mathrm{LV}}u_{\mathrm{v}}-A_{\mathrm{i}}\tau_{\mathrm{i,z}}c_{\mathrm{z}}(\phi) \tag{3.25}$$

It is possible to use the Eqs. (3.3), (3.4) and (3.8) in order to rearrange the Eq. (3.28). Consequently, Eqs. (3.26) and (3.27) are derived.

$$\rho_{\mathrm{V}}\frac{\partial\left(A_{\mathrm{V,z}}u_{\mathrm{V}}^2\right)}{\partial z}\mathrm{d}z+\rho_{\mathrm{V}}\frac{\partial\left(A_{\mathrm{V,\theta}}v_{\mathrm{V}}u_{\mathrm{V}}\right)}{r\partial\theta}r\mathrm{d}\theta=-A_{\mathrm{V,z}}\frac{p_{\mathrm{V}}}{\partial z}\mathrm{d}z+\mathrm{d}\dot{m}_{\mathrm{LV}}u_{\mathrm{V}}-A_{\mathrm{i}}\tau_{\mathrm{i,z}}c_{z}(\phi) \tag{3.26}$$

$$\rho_{\mathrm{V}}u_{\mathrm{V}}^2r\frac{\partial r}{\partial z}+\rho_{\mathrm{V}}r^2u_{\mathrm{V}}\frac{\partial u_{\mathrm{V}}}{\partial z}+\rho_{\mathrm{V}}v_{\mathrm{V}}u_{\mathrm{V}}\frac{\partial r}{\partial\theta}+\rho_{\mathrm{V}}ru_{\mathrm{V}}\frac{\partial v_{\mathrm{V}}}{\partial\theta}+\rho_{\mathrm{V}}rv_{\mathrm{V}}\frac{\partial u_{\mathrm{V}}}{\partial\theta}=$$

$$-\frac{r^2}{2}\frac{\partial p_{\mathrm{V}}}{\partial z}+\frac{\dot{q}\cdot R}{h_{\mathrm{LV}}}u_{\mathrm{V}}-r\tau_{\mathrm{i,z}}c_{\mathrm{z}}(\phi) \tag{3.27}$$

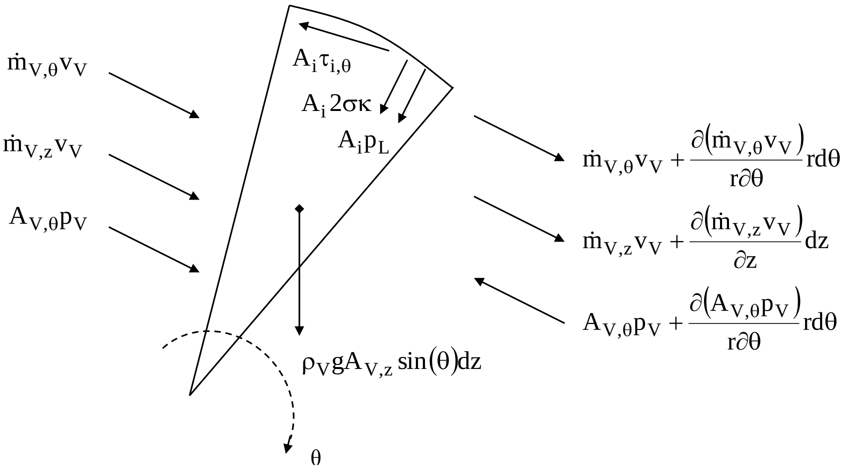

Figure 3.8: Momentum balance in the tangential direction for the vapour phase.

3.1.9 Momentum equation in the tangential direction for the vapour phase

In Fig. 3.8, the forces acting on the vapour phase infinitesimal control volume in tangential direction are represented. The following equation is derived.

$$\begin{aligned}\rho_V\frac{\partial\left(A_{V,\theta}v_V^2\right)}{r\partial\theta}r\mathrm{d}\theta+\rho_V\frac{\partial\left(A_{V,z}u_V v_V\right)}{\partial z}\mathrm{d}z=-\frac{\partial\left(A_{V,\theta}p_V\right)}{r\partial\theta}r\mathrm{d}\theta+\\ A_i 2\sigma\kappa\sin(\psi)+A_i p_L\sin(\psi)+\rho_V g A_{V,z}\sin(\theta)\mathrm{d}z+A_i\tau_{i,\theta}c_\theta(\psi)\end{aligned}\tag{3.28}$$

Using Eqs. (3.3), (3.5) and (3.8), it is possible to obtain:

$$\rho_V\frac{\partial\left(A_{V,\theta}v_V^2\right)}{r\partial\theta}r\mathrm{d}\theta+\rho_V\frac{\partial\left(A_{V,z}u_V v_V\right)}{\partial z}\mathrm{d}z=-A_{V,\theta}\frac{\partial p_V}{r\partial\theta}r\mathrm{d}\theta+\rho_V g A_{V,z}\sin(\theta)\mathrm{d}z+A_i\tau_{i,\theta}c_\theta(\psi)\tag{3.29}$$

$$\begin{aligned}\rho_V v_V^2\frac{\partial r}{\partial\theta}+2\rho_V r v_V\frac{\partial v_V}{\partial\theta}+\rho_V u_V v_V r\frac{\partial r}{\partial z}+\rho_V\frac{r^2}{2}v_V\frac{\partial u_V}{\partial z}+\rho_V\frac{r^2}{2}u_V\frac{\partial v_V}{\partial z}=\\ -r\frac{\partial p_V}{\partial\theta}+\rho_V g\frac{r^2}{2}\sin(\theta)+r\tau_{i,\theta}c_\theta(\psi)\end{aligned}\tag{3.30}$$

It should be noted that the sign of the interfacial frictional shear stress in Eqs. (3.28), (3.29) and (3.30) is consistent with the experimental and numerical studies of Sutharshan et al. [92], Paras and Karabelas [63], Flores et al. [85], van't Westende et al. [95], Höhne et al. [98].

3.2 Treatment of the frictional shear stresses

3.2.1 Liquid-wall frictional shear stress

Most authors, among which Whang Na and Chung [71], Kim and Mudawar [73, 74], Nebuloni and Thome [82], Da Riva et al.[83], used the Newton Law for fluid flow in order to calculate the friction between liquid film and wall. Alipchenkov et al. [68] and Revellin and Thome [69] utilized single-phase correlations. In the present study, in order to propose a more simple model, single-phase correlations are used. In the axial direction, the frictional shear stress can be computed as follows:

$$\tau_{\mathrm{LW,z}} = f\frac{1}{2}\rho_{\mathrm{L}}u_{\mathrm{L}}^2 \tag{3.31}$$

The friction factor f is computed with the *Haigen-Poiseulle*'s equation and the *Blasius*' equation, for laminar and turbulent flow respectively.

$$f = \begin{cases} 16/Re, & \text{if } Re < 2300; \\ 0.0791Re^{-0.25}, & \text{if } Re \geq 2300. \end{cases} \tag{3.32}$$

The Reynolds number $Re_{\mathrm{L,z}}$ and the hydraulic diameter $D_{\mathrm{L,z}}$, to be used in Eqs. (3.31) and (3.32), are given in Eqs. (3.33) and (3.34).

$$Re_{\mathrm{L,z}} = \frac{\rho_{\mathrm{L}}u_{\mathrm{L}}D_{\mathrm{L,z}}}{\mu_{\mathrm{L}}} \tag{3.33}$$

$$D_{\mathrm{L,z}} = 2\left(\frac{R^2 - r^2}{R}\right) \tag{3.34}$$

In the tangential direction, the frictional shear stress is given by:

$$\tau_{\mathrm{LW,\theta}} = f\frac{1}{2}\rho_{\mathrm{L}}v_{\mathrm{L}}^2 \tag{3.35}$$

Eqs. (3.36) and (3.37) respectively assign the values for the Reynolds number $Re_{\mathrm{L,\theta}}$ and the hydraulic diameter $D_{\mathrm{L,\theta}}$ to be used in Eqs. (3.35) and (3.32).

$$Re_{\mathrm{L,\theta}} = \frac{\rho_{\mathrm{L}}v_{\mathrm{L}}D_{\mathrm{L,\theta}}}{\mu_{\mathrm{L}}} \tag{3.36}$$

$$D_{\mathrm{L,\theta}} = 4(R - r) \tag{3.37}$$

3.2.2 Interfacial shear stress

The interface is not smooth, but presents waves and tends to act as a rough surface for both the vapour core and the liquid film. The Moeck's correlation [54] was obtained for disturbance wave region in air-water flow. Fukano and Furukawa [44] proposed a correlation for vertical air-water flows. Wang and Rose [81] and Nebuloni and Thome [82] followed the approach of [99], including a correction factor for the condensation effect. Alipchenkov et al. [68] used a modified Wallis' correlation. Kim and Mudawar [73, 74] utilized the correlation of [100]. Kishore and Jayanti [67] and Belt et al. [101] used a sand-grain roughness approach, but fitting the sand-grain roughness k_s in a narrow range of experimental data. The single-phase correlation for laminar flow is used by Whang Na and Chung [71]. Fore et al. [53] proposed a modified Wallis' correlation in order to better predict the interfacial friction factor. in transition roughness regime. In the studies of Schubring and Shedd [50, 61], a correlation for fully-rough regime was used. although the interfacial shear stress is an active field of research, the most reliable correlation, for operational conditions and working fluids analysed in this paper, seems to be the Wallis' one. For the axial direction, the interfacial shear stress is defined as follows:

$$\tau_{\mathrm{i,z}} = f_{\mathrm{i}} \frac{1}{2} \rho_{\mathrm{V}} (u_{\mathrm{V}} - u_{\mathrm{i}}) \left| u_{\mathrm{V}} - u_{\mathrm{i}} \right| \tag{3.38}$$

According to Wallis, the interface velocity u_i can be computed as

$$u_{\mathrm{i}} = 2 u_{\mathrm{L}} \tag{3.39}$$

The interfacial friction factor f_i results to be a function of the liquid film thickness and the friction factor of the vapour core.

$$f_{\mathrm{i}} = f \left(1 + 300 \frac{\delta}{D} \right) \tag{3.40}$$

In Eq. (3.40), the friction factor f is computed as in Eq. (3.32) on condition that the velocity u_{V}, the thermodynamic properties of the vapour core and the hydraulic diameter defined $D_{\mathrm{V,z}}$ in Eq. (3.41) are used.

$$D_{\mathrm{V,z}} = 2r \tag{3.41}$$

In the tangential direction, it is assumed that the interface velocity is null. Hence, the interfacial shear stress is defined as:

$$\tau_{\mathrm{i},\theta} = f_{\mathrm{i}} \frac{1}{2} \rho_{\mathrm{V}} v_{\mathrm{V}}^2 \tag{3.42}$$

The interfacial friction factor is given in Eq. (3.40). The friction factor of the vapour core is computed using the velocity v_{V} and the hydraulic diameter given in Eq. (3.43).

$$D_{\mathrm{V},\theta} = 4r \tag{3.43}$$

Chapter 4

NUMERICAL ANALYSIS AND VALIDATION

4.1 Numerical method

Eqs. (3.8), (3.13), (3.16), (3.20), (3.24), (3.27) and (3.30) compose a system of 7 non-linear differential equations in 7 unknowns (r, u_L, v_L, p_L, u_V, v_V, p_V). Such a system can be solved with the aid of an iterative numerical method. In the present work, the Finite Difference method is used [102]. The domain is subdivided in a mesh of $n_z \cdot n_\theta$ nodal points, being n_z and n_θ the number of nodal points along the z-axis and the θ-axis, respectively. In Fig. 4.1, a representation of such mesh is shown. The quantities i and j enumerate the nodal points along the z-axis and the θ-axis, respectively. The derivatives appearing in the aforementioned equations are computed with the backward and central difference approximations, depending on the position of the nodal points, as indicated in Table 4.1. It is worth mentioning that a boundary condition has been set in the inlet section, assuming an axial-symmetric liquid film distribution, which is computed by means of the the Rouhani-Axelsson's correlation [20]. The discretized form of the fundamental equations are applied on each node in order to compose an linear system. Three features are investigated for the purpose of verify the reliability of the solution of such a system: accuracy of solution, ill-conditioning, numerical convergence and stability.

4.1.1 Accuracy of solution

The linear system can be written in matrix form as

$$\mathbf{A}\mathbf{x} = \mathbf{B} \tag{4.1}$$

where **A**, **x** and **B** are the matrix of coefficients, the column vector of unknowns and the column vector of known coefficients. For sake of completeness, the sparsity patterns of the matrix **A** for the nodal points in one cross-section and for the nodal points in four neighbouring cross-sections are shown in Fig. 4.2 and Fig. 4.3, respectively.

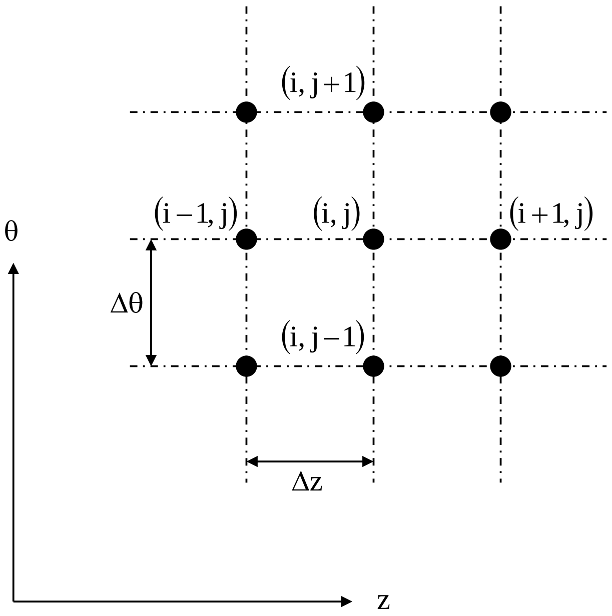

Figure 4.1: Mesh of nodal points for the Finite Difference method.

Approximation	Discrete operator	Truncation error	Nodal points
Backward	$\frac{\mathrm{x}(i,j)-\mathrm{x}(i-1,j)}{\Delta z}$	Δz	$i = n_z$
Central	$\frac{\mathrm{x}(i+1,j)-\mathrm{x}(i-1,j)}{2\Delta z}$	Δz^2	$i = 2, n_z - 1$
Central	$\frac{-\mathrm{x}(i+2,j)+8\mathrm{x}(i+1,j)-8\mathrm{x}(i-1,j)+\mathrm{x}(i-2,j)}{12\Delta z}$	Δz^4	$3 \leq i \leq n_z - 2$
Central	$\frac{-\mathrm{x}(i,j+2)+8\mathrm{x}(i,j+1)-8\mathrm{x}(i,j-1)+\mathrm{x}(i,j-2)}{12\Delta z}$	$\Delta\theta^4$	$1 \leq j \leq n_\theta$

Table 4.1: Derivative discrete operators for the Finite Difference method.

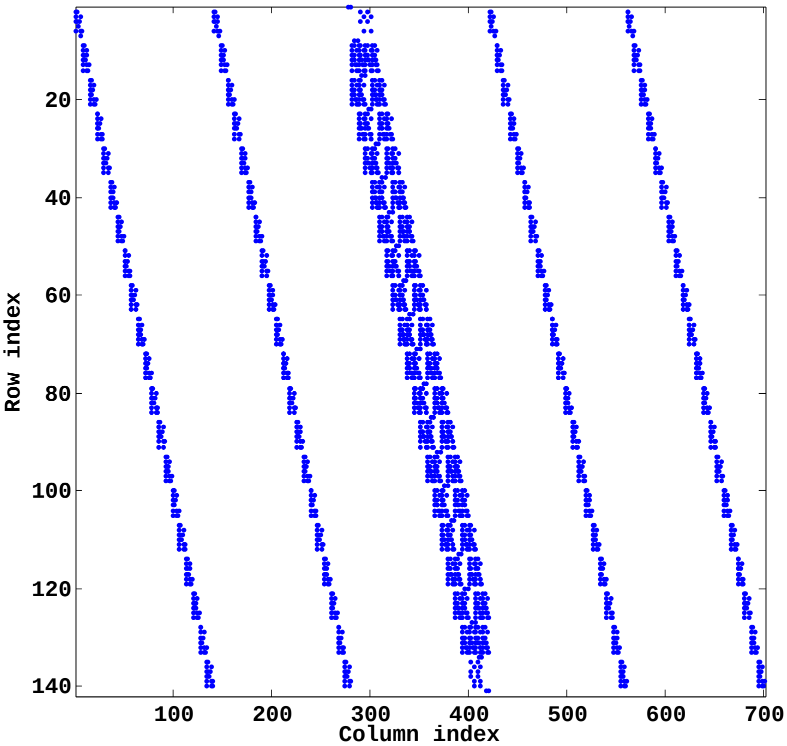

Figure 4.2: Sparsity pattern of the matrix of coefficients for the nodal points in one cross-section.

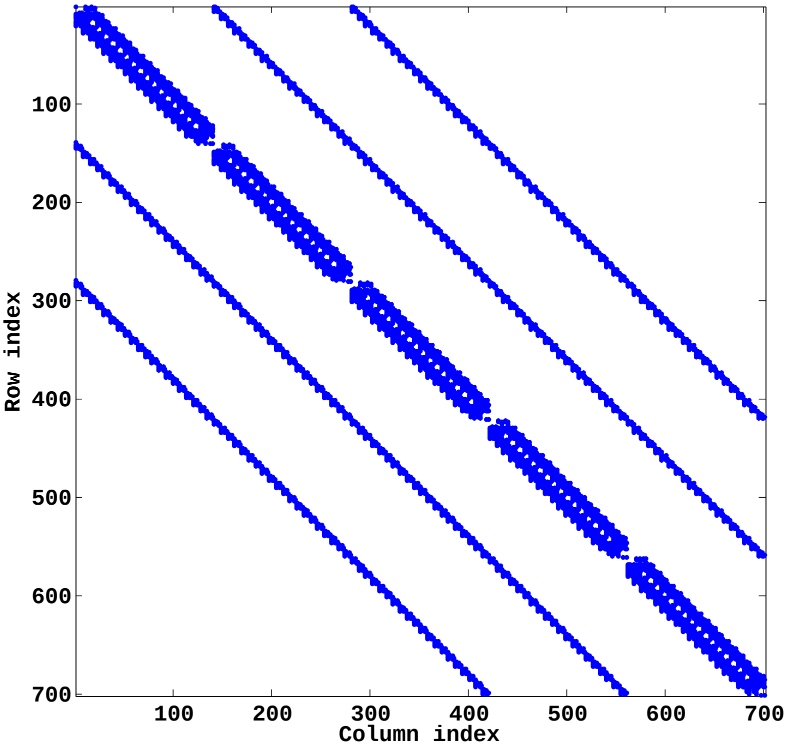

Figure 4.3: Sparsity pattern of the matrix of coefficients for the nodal points in four neighbouring cross-sections.

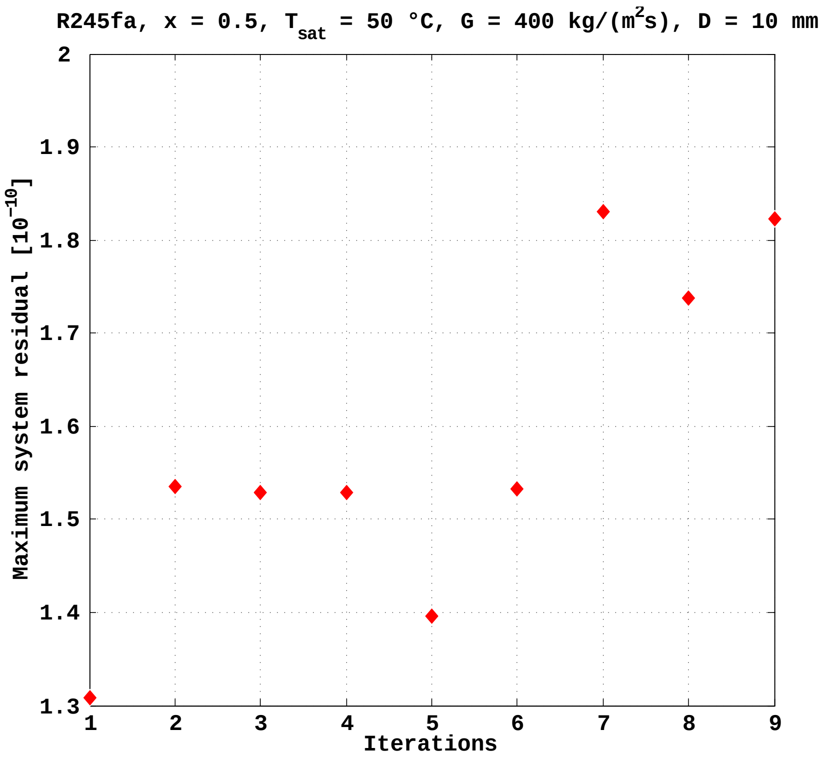

Figure 4.4: MSR against the number of iterations.

In Fig. 4.2, it is possible to note that the first and the last points in the central group, which are the nodes for the top tube and bottom tube, are characterised by symmetry condition for the unknowns r, u_{L}, p_{L}, u_{V}, p_{V} and asymmetry condition for the unknowns v_{L}, v_{V}.

Once the solution of the unknowns in the column vector $\mathbf{x}$ has been found, it is possible to compute the system residuals SR as follows:

$$SR = \mathbf{Ax\text{-}B} \tag{4.2}$$

It is worth mentioning that the matrix of coefficients $\mathbf{A}$ is a function of the unknowns in the column vector $\mathbf{x}$ because of the non-linearity of the fundamental equations. The linear system has to be solved with an iterative method. In order to obtain an accurate solution, the system residuals have to approach the zero value. In Fig. 4.4, the maximum system residual (MSR) is reported against the number of iterations for a certain operational condition. The MSR shows an order of magnitude of $1-2\cdot 10^{-10}$, ensuring the excellent accuracy of solutions. Moreover, the solution exists and it is unique, proving that the problem is well-posed.

4.1.2 Ill-conditioning

In linear systems such as Eq. (4.1), the condition number is a measure of the variation in the output values for a small change of the input values. Linear systems are well-

Condition number	$n_z = 500$	$n_z = 1700$
2D annular flow model	$4.0413 \cdot 10^{15}$	$1.6065 \cdot 10^{17}$
Hilbert	$4.4417 \cdot 10^{20}$	$1.2795 \cdot 10^{21}$
Poisson	$4.1357 \cdot 10^{4}$	$1.4093 \cdot 10^{5}$

Table 4.2: Condition numbers estimation and comparison.

conditioned if the condition number is sufficiently near the unit value, otherwise they are said to be ill-conditioned. The condition number is greater or equal to 1 and it is a property of the matrix of coefficients **A**. Hereinafter, the condition number are calculated by means of the 1-norm condition estimator of Hager. In Table 4.2, the condition numbers are reported for the matrix of coefficients **A** of the two-dimensional annular flow model, Hilbert matrix, and 5-point Poisson matrix. The Hilbert matrix has been chosen because it is a classical example of ill-conditioned system, whereas the Poisson matrix has been investigated for sake of comparison to a well-conditioned problem. Considering a number of elements for the Hilbert matrix equal to the square root of the number of non-zero values in the two-dimensional model matrix, it can be deducted that the two-dimensional annular flow problem is not ill-conditioned. As a matter of fact, the difference between the two condition numbers is about 4 orders of magnitude. However, by comparison with the Poisson matrix, the solution of such a model may be subject to rounding error. Nevertheless, such an approximation is acceptable enough for the purpose of this study.

4.1.3 Numerical convergence and stability

The numerical convergence has been examined through a monitoring of the solution of the linear system against the variation of the number of nodal points. The stability of the numerical method is evaluated with the maximum relative residual (MRR), defined as:

$$MRR = max\left(\frac{\mathbf{x}_{\text{iter}} - \mathbf{x}_{\text{iter-1}}}{\mathbf{x}_{\text{iter-1}}}\right) \tag{4.3}$$

In Eq. (4.3), y indicates the iteration. Considering a trade-off between accuracy of the solution and the computational time, the value of the maximum relative residual had been set to 10^{-2} as stop criterion. For sake of example, a convergence plot of the maximum relative residual against the number of iterations is shown in Fig. 4.5 on varying the number of nodal points. It results that the more dense the grid, the more stable the solution.

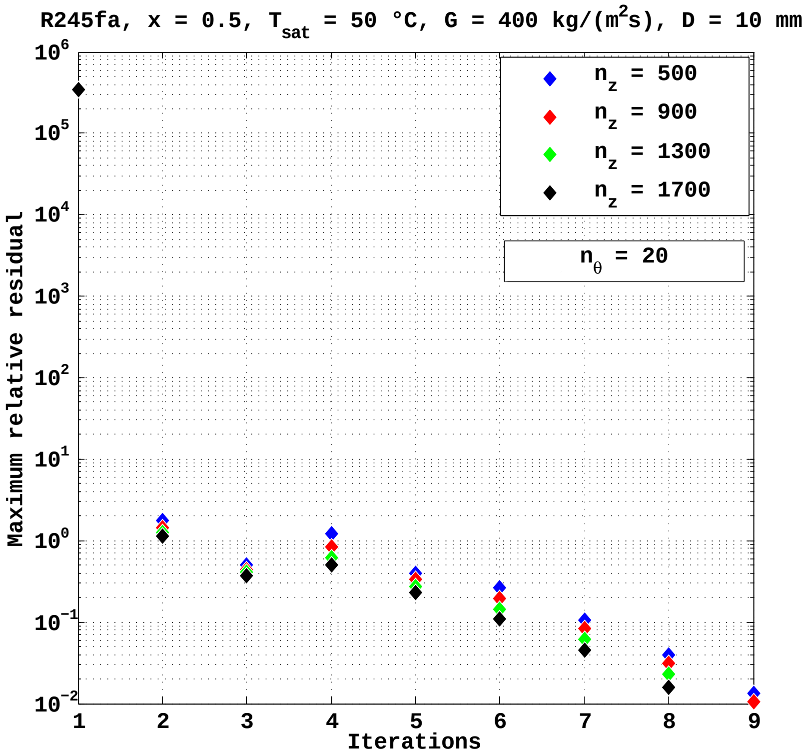

Figure 4.5: MRR against the number of iterations.

4.2 Validation of the model

4.2.1 Pressure drop experimental database description

The model has been validated against an experimental pressure drop database from Padilla et al. [103], Mastrullo et al. [104] and Revellin and Thome [105]. The details of the database are summarized in Table 4.3. It consists of 107 data points, 60 for conventional channels split among R134a, R410A and R1234yf, 23 for the carbon dioxide, and 24 for microchannels. It is worth noting that the database include operational conditions in which the stratification of the liquid film is significative. In Fig. 4.6, the distribution of the data points against the operational variables and the density ratio is shown. The data points against the mass flux and the saturation temperature are well-distributed. The vapour quality shows the typical transition from higher values in conventional channel to lower values in microchannels. It is worth to noting that the distribution of the density ratio is staggered for conventional channel data points. Such behaviour is a consequence of the different critical temperatures of the fluids which compose the database.

4.2.2 Pressure drop comparison between model and experimental data

In Fig. 4.7, it is shown the discrepancy between the solutions of the model and the experimental data for the whole pressure drop database. The RME, the MRE and the P20 results to be 8.72 %, 24.94 % and 94.4 %, respectively, ensuring the validity of

D $[mm]$	Fluid	G $[kg/(m^2s)]$	T [°C]	x [–]
7.9 - 10.85	R134a	299.8 - 948.7	10.31 - 20.35	0.4034 - 0.6170
	R1234yf	300.5 - 1147.9	14.88 - 15.78	0.3939 - 0.6051
	R410A	368.8 - 1667.9	5.761 - 21.21	0.3970 - 0.6271
6	R744	300.0 - 350.0	4.50 - 5.10	0.4180 - 0.840
0.517	R134a	475.2 - 1986.9	18.79 - 29.35	0.0849 - 0.4000

Table 4.3: Experimental pressure drop database.

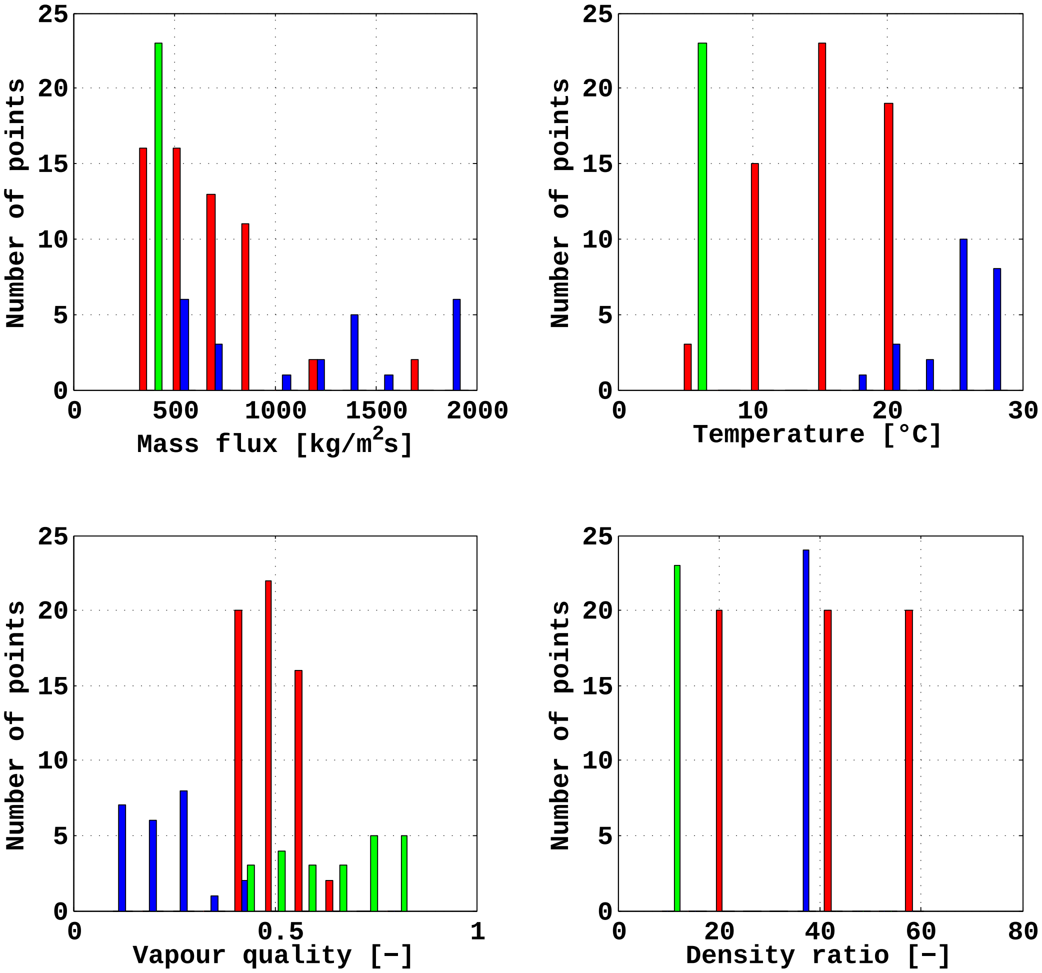

Figure 4.6: Data points distribution against the operational variables (Red: conventional channels; Blue: microchannels; Green: carbon dioxide).

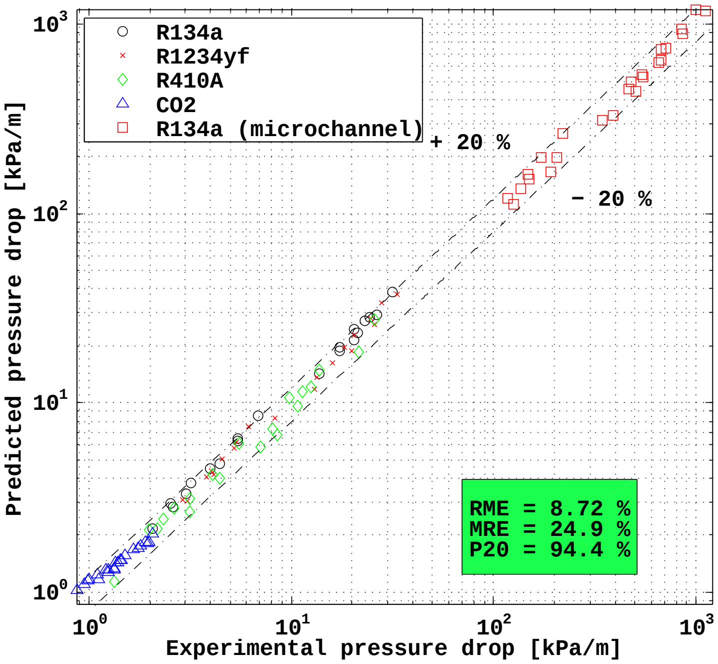

Figure 4.7: Comparison between the solutions of the model and the experimental data for the pressure drop.

the model. From the scatter plot, it seems that the model slightly overestimates the experimental data. The authors share this opinion because this behaviour is due to the absence of equations which take into account the entrainment of liquid droplets. Indeed, the overestimation does not occur for R410A data points. The density ratio and the surface tension, the main thermodynamic properties affecting the entrainment [38, 106, 107], are lower for R410A than the other two refrigerants, according to the operational conditions described previously. This behaviour is also verified with the carbon dioxide, which is the working fluid with the more intense stratification in the selected database. Regarding the pressure drop in microchannels, it appears that the discrepancy between the model and experiments does not follow any particular behaviour.

4.2.3 Liquid film thickness experimental database description

A comparison has been carried out between experimental and predicted liquid film thickness. The experimental data points has been choosen from the database of Luninski [108] and they are composed by 10 operational conditions for flow of air-water mixture at room temperature. The details of the database are given in Table 4.4.

4.2.4 Liquid film thickness comparison between model and experimental data

In Fig. 4.8, the comparison between experimental data and model predictions is shown. It is worth mentioning that liquid film measurements is a diffcult task. A study carried

D $[mm]$	Fluid	J_L $[m/s]$	J_V $[m/s]$	p $[kPa]$
8.15, 9.85, 12.30	air - water	0.16 - 0.40	10 - 40	100

Table 4.4: Experimental liquid film thickness database.

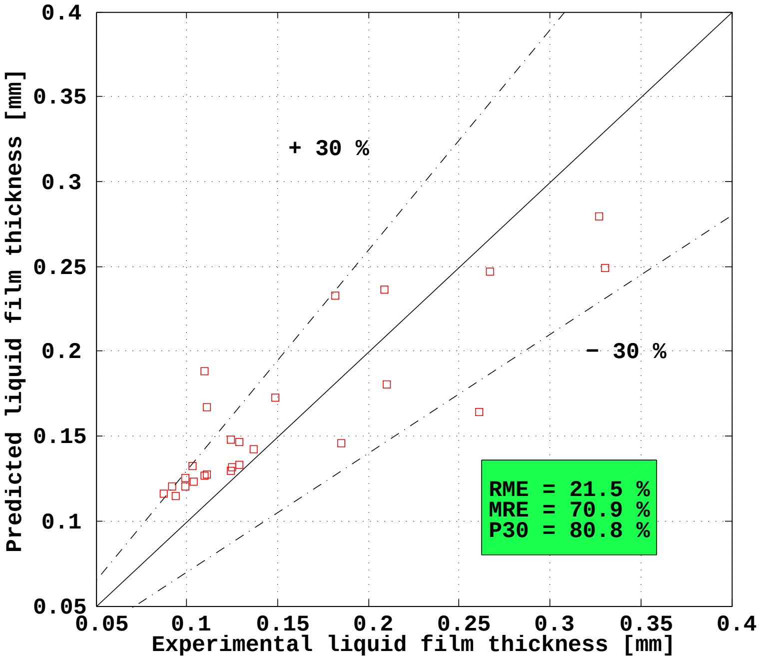

Figure 4.8: Liquid film thickness comparison between the solutions of the model and the experimental data for air-water.

out by Damsohn and Prasser [109] with the electrical conductance method shows that, for thin liquid film in air-water annular flow pattern, the measurement error may amount to 50 %. Recently, Ashwood et al. [110], using a micro-scale PIV measurement technique, declared a maximum uncertainty in the wall shear stress of 15 %, although it is not clear how this uncertainty propagates in the liquid film thickness. Regarding this comparison, it is undeniable that the discrepancy is significantly large for some measurements, since the MRE results to be 70.9 %. However, the model may comprehensively be considered as a good predictor for the liquid film thickness, namely RME = 21.5 % and P30 = 80.8 %.

Chapter 5

MODEL ASSESSMENT AND APPLICATION

5.1 Liquid film thickness and pressure drop

The pressure drop in annular flow is usually computed by means of an one-dimensional force balance on the vapour core, provided that the average liquid film thickness and the interfacial shear stress are known. Hereinafter, pressure drop is intended to be calculated solving the two-dimensional and founding the $\mathrm{d}p/\mathrm{d}z$ in the liquid phase.

A comparison about the calculation of the liquid film thickness between the two-dimensional model and the Hurlburt's and Newell's correlation [40] is reported in Fig. 5.1. It is possible to note that the two-dimensional model and the Hurlburt's and Newell's correlation are in satisfactory agreement in the prediction of the liquid film thickness in tube top and average values, whereas a certain difference results for the tube bottom values. However, it is clear that the two-dimensional model tends to overestimate the liquid film thickness. In more detail, the difference in the solution between the the methods increases for lower values of the saturation temperature (figures 5.1a and 5.1b) and for higher values of the mass flux (figures 5.1c and 5.1d). The two-dimensional model presents such behaviours because it neglects the influence of two peculiar phenomena of annular flow, namely the entrainment of liquid droplets and the disturbance waves. These events exhibit a growing influence on annular flow as the difference between liquid film flow rate and the critical liquid mass flow rate for the disturbance waves incipience increases [111, 112]. In Table 5.1, the liquid phase mass flux G_{L}, the critical mass flux for the onset of entrainment G_{LFC} and the entrainment mass flux G_{LE} are calculated for the fluids and operational conditions shown in Fig. 5.1. According to the previous considerations, the greater the entrainment mass flux, the more the discrepancy between the two methods.

Under the same operational conditions, a comparison with a pressure drop correlation has been carried out in Fig. 5.2. Among numerous pressure drop correlations for two-phase flow [113], the Müller-Steinhagen's and Heck's correlation has been chosen because of its good accuracy in the pressure drop prediction for refrigerants in the operational

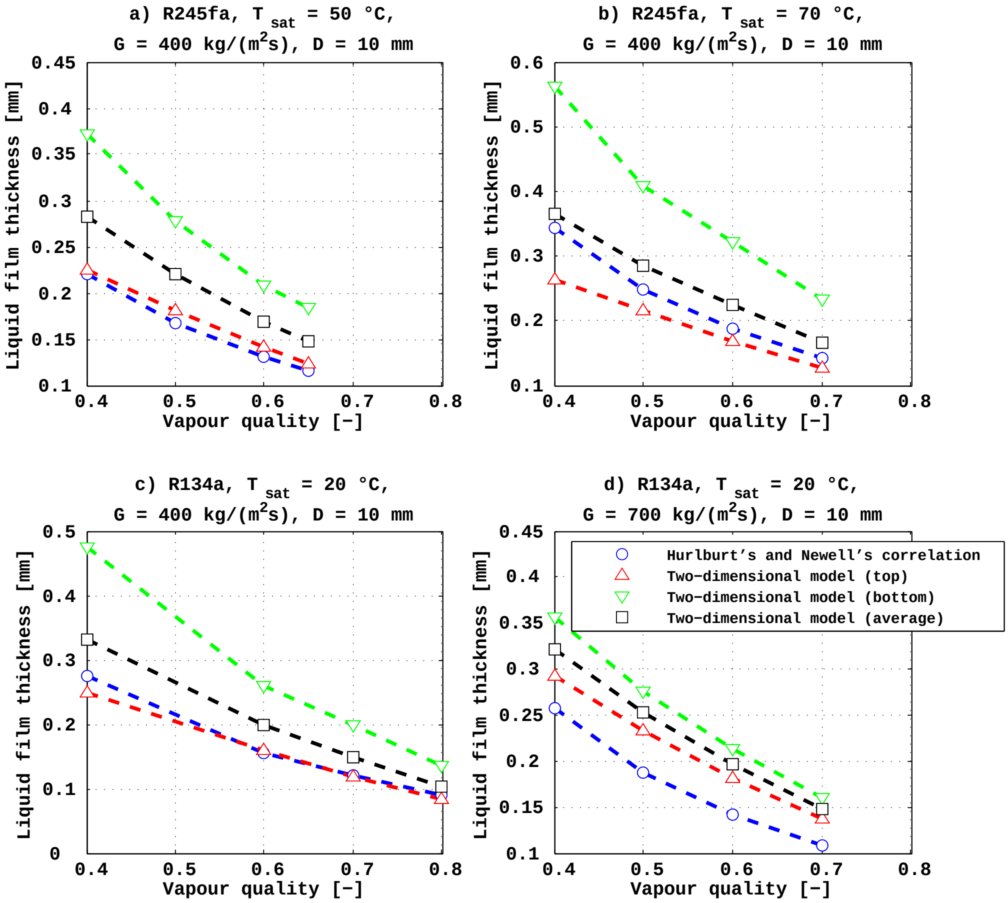

Figure 5.1: Comparison on the liquid film thickness correlation between the two-dimensional model and the Hurlburt's and Newell's correlation.

Case	$G_L[kg/m^2s]$	$G_{LFC}[kg/m^2s]$	$G_{LE}[kg/m^2s]$
a)	160	11.5	0.4735
b)	160	8.97	0.3579
c)	160	8.42	0.3988
d)	280	8.42	1.0089

Table 5.1: Mass flux, critical mass flux and entrainment rate of the liquid phase for the cases shown in Fig 5.1, calculated at vapour quality 0.6.

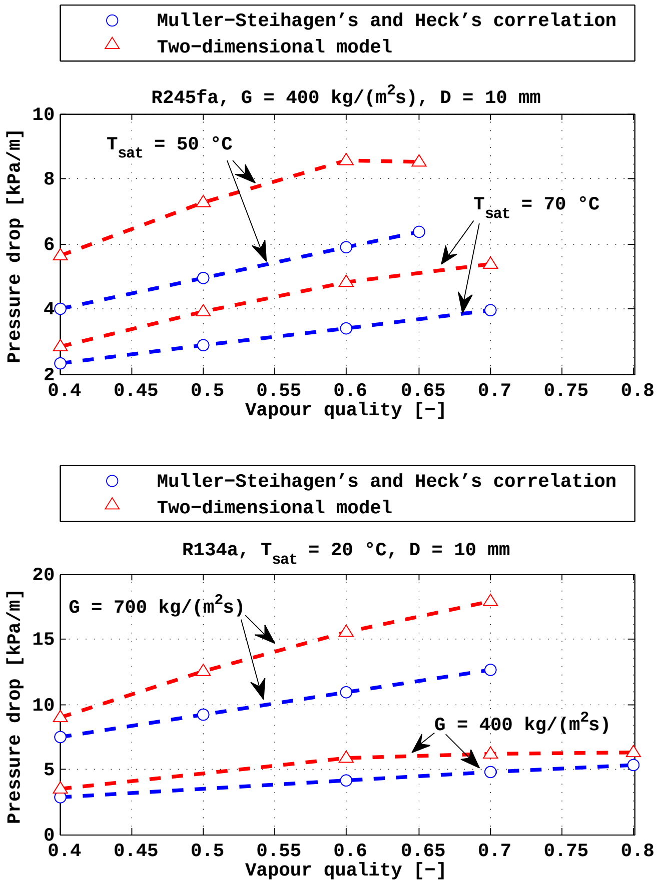

Figure 5.2: Comparison on the pressure drop prediction between the two-dimensional model and the Müller-Steinhagen's and Heck's correlation.

conditions and channel sizes of interest. As expected, the pressure drop prediction of the two-dimensional model shows greater values in comparison to the Müller-Steinhagen's and Heck's correlation. The discrepancy between the two methods tends to decrease at relatively low pressure drop conditions, namely at higher values of saturation temperature and lower values of mass flux.

Fig. 5.3 reports the influence of the gravity acceleration on the pressure drop. The less the gravity acceleration, the less the pressure drop. This trend can be explained as follows. The asymmetry in the liquid film distribution causes an asymmetry in the liquid-wall frictional shear stress and in the interfacial shear stress. This effect can be deducted from Fig. 5.4. whereas the former is decreased with the stratification, the latter is increased. It is worth noting that axial liquid velocity is only barely affected by the stratification. Because of the high values of the void fraction, the increase in the interfacial shear stress rules against the decrease in the liquid-wall frictional shear stress. Hence, the stratification causes an accretion on the pressure drop. Nevertheless, for R410A at 40 °C of saturation temperature and 400 $kg/(m^2 \cdot s)$ of mass flux, the relative difference on the pressure drop between normal gravity and micro-gravity equals -3.9 %. Therefore,

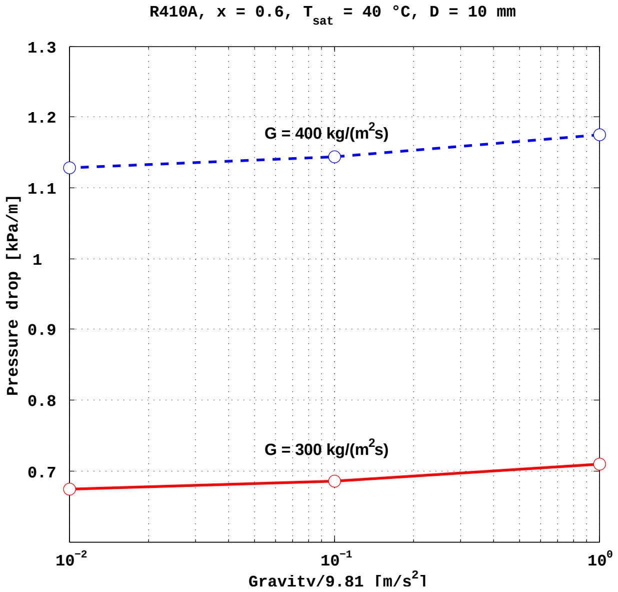

Figure 5.3: Influence of the gravity acceleration on the pressure drop.

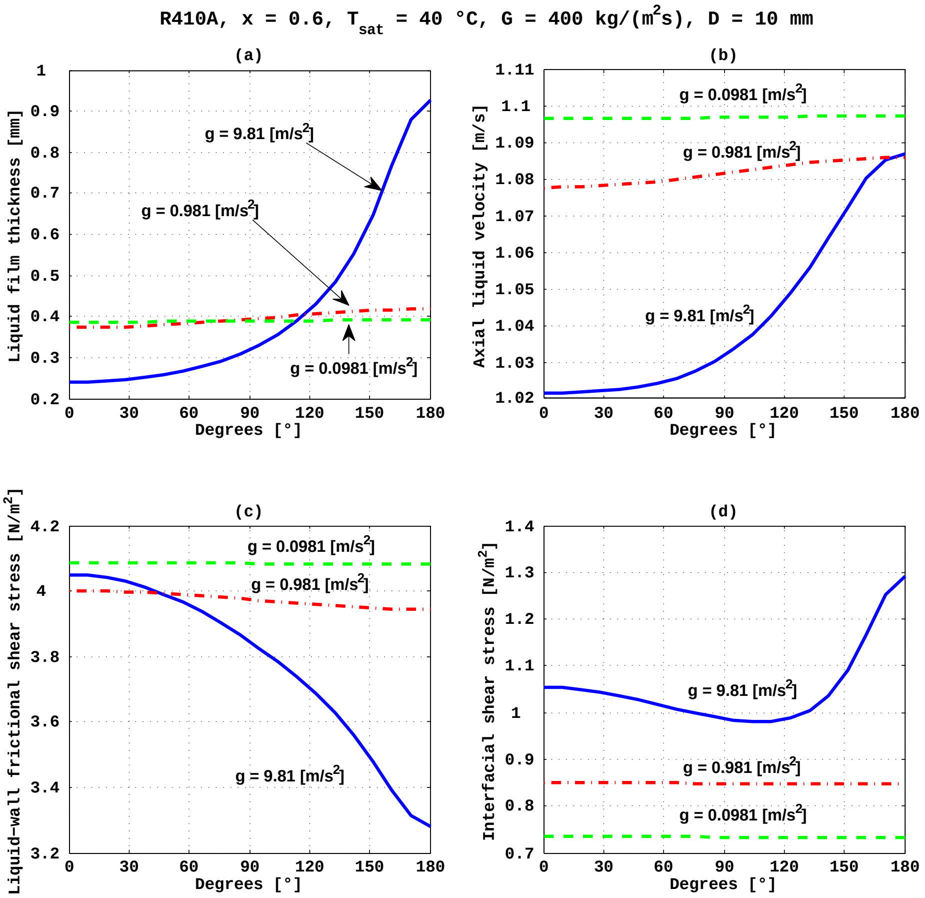

Figure 5.4: Influence of the gravity acceleration on (a) liquid film distribution, (b) axial liquid velocity, (c) liquid-wall frictional shear stress and (d) interfacial shear stress.

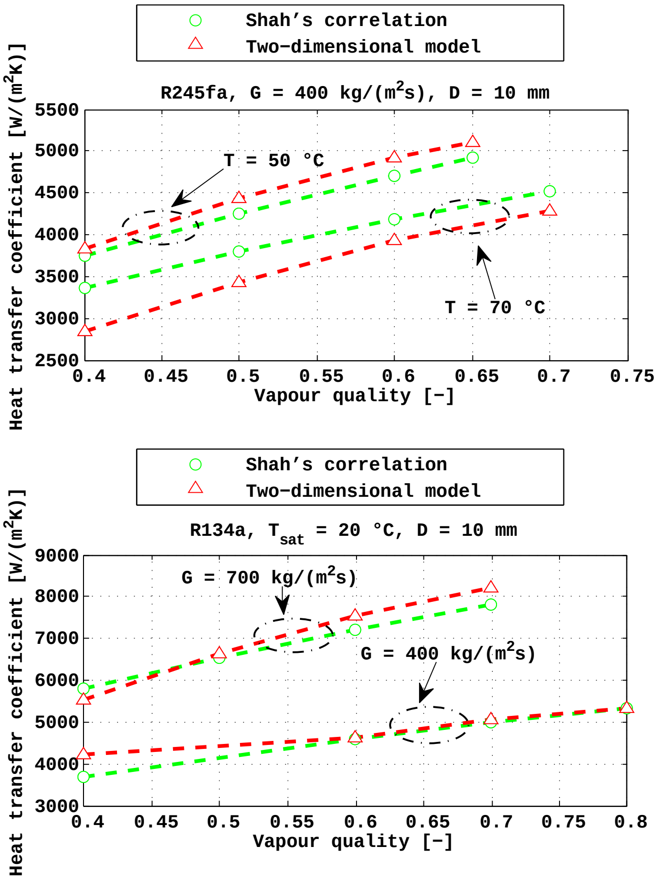

Figure 5.5: Comparison on the heat transfer prediction between the two-dimensional model and the Shah's correlation.

the influence of the stratification on the pressure drop losses significance as the interfacial shear stress increases.

5.2 Heat transfer coefficient

The liquid film distribution causes also a variation on the heat transfer coefficient in the cross-section. It is worth recalling the definition of heat transfer coefficient and Nusselt number in two-phase flow, given respectively by the following equations:

$$h = \frac{\dot{q}}{(T_{\mathrm{W}} - T_{\mathrm{sat}})} \tag{5.1}$$

$$Nu = \frac{h\delta}{k_{\mathrm{L}}} \tag{5.2}$$

It is worth mentioning that, once the liquid film distribution is known, the calculation of the heat transfer coeffcient is possible by using Eqs. (2.60) and (2.62).

A comparison has been carried out in Fig. 5.5 between the cross-sectional average value of heat transfer coefficient obtained by the two-dimensional model and the Shah's correlation [114], which is one of most accurate for condensing flow. The reason that have led to the selection of a correlation for condensation is the absence of the nucleation and entrained liquid droplets phenomena in the two-dimensional model. It is well-known that such events do not occur in condensing annular flow, whereas are peculiar during evaporation. The agreement between the two methods results to be very satisfactory.

In Fig. 5.6, the liquid film distribution, the dimensionless liquid film thickness, the liquid Nusselt number and the local heat transfer coefficient are shown on varying the saturation temperature of the working fluid. The liquid film stratification increases as the saturation temperature increases, because of the lower values of density ratio between the liquid and the vapour phases. Despite the variation of the dimensionless liquid film thickness may suggest a strong convection at the tube bottom, the local heat transfer increases moving toward the tube top. For instance, in the conditions described in Fig. 5.6, with R134a at 60 °C of saturation temperature, the top heat transfer coefficient and the bottom heat transfer coefficient yield a discrepancy against the average heat transfer coefficient of 3.52 % and -7.15 %, respectively. It is clear that such a discrepancy grows in magnitude as the saturation temperature increases. In Table 5.2, the liquid thermal conductivity for some working fluids is reported on varying the saturation temperature. The difference between the heat transfer coefficient curves in Fig. 5.6d are mainly due to the decrease of the liquid thermal conductivity against the saturation temperature.

The influence of the channel diameter on liquid film distribution, dimensionless liquid film thickness, liquid Nusselt number and local heat transfer coefficient is reported in Fig. 5.7. As expected, the stratification losses significance for lower values of the channel diameter. It is worth noting that higher values of the heat transfer coefficient for the R245fa respect to the R134a are mainly due to the lower values of liquid film thickness. Indeed, the liquid thermal conductivity and the liquid Nusselt number are very similar for these two fluids. The tangential variation of the heat transfer coefficient shows the same trend encountered previously. For sake of instance, in the same conditions reported in Fig. 5.7, the top heat transfer coefficient for R245fa in 10 mm channel diameter presents a relative difference against the average value of 1.47 %, whereas the bottom heat transfer coefficient diverges from the average value by -1.91 %.

In Fig. 5.8, the liquid film distribution, the dimensionless liquid film thickness, the liquid Nusselt number and the local heat transfer coefficient are shown on varying the

k_{L} $[10^{-3} W/(mK)]$	$T_{\mathrm{sat}} = 30°\mathrm{C}$	$T_{\mathrm{sat}} = 50°\mathrm{C}$	$T_{\mathrm{sat}} = 70°\mathrm{C}$
R134a	79.0	70.4	61.7
R245fa	86.5	80.2	73.7

Table 5.2: Liquid thermal conductivity for some working fluids on varying the saturation temperature.

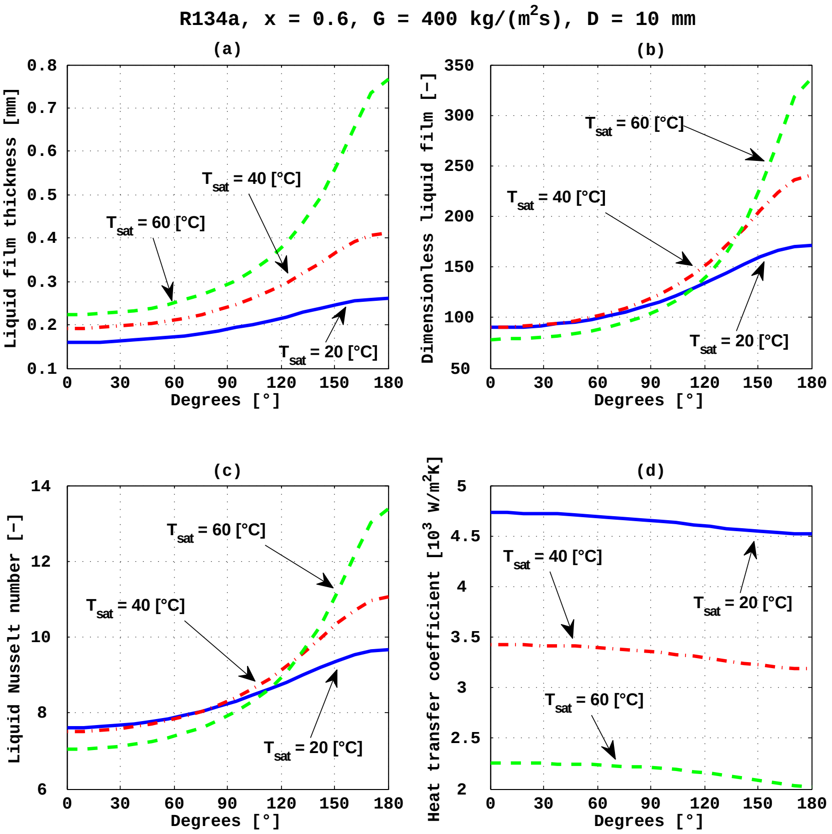

Figure 5.6: Influence of the saturation temperature on (a) liquid film distribution, (b) dimensionless liquid film thickness, (c) liquid Nusselt number and (d) local heat transfer coefficient.

vapour quality. It is possible to note that the heat transfer coefficient approaches to a maximum at about 0.81 of vapour quality. The reason in the decrease of the heat transfer rate may be explained by means of the liquid film thermal resistances in the laminar sublayer, buffer layer and turbulent core. Such thermal resistances are shown in Fig. 5.8, for the same operational conditions and working fluid of Fig. 5.8. Three important features can be deducted:

- The magnitude of the turbulent core's thermal resistance is negligible compared to the laminar sublayer's and the buffer layer's. This observation leads to the consequence that the conduction mechanism dominates on the convection in the conditions here analysed. Therefore, the stratification of the liquid film ensures a decrease of the heat transfer coefficient toward the tube bottom.

- A positive variation of the heat transfer coefficient toward the tube bottom may only be possible for great variation of the interfacial shear stress in the tangential direction. This event is realised in conditions of high values of ratio between bottom film thickness and channel diameter.

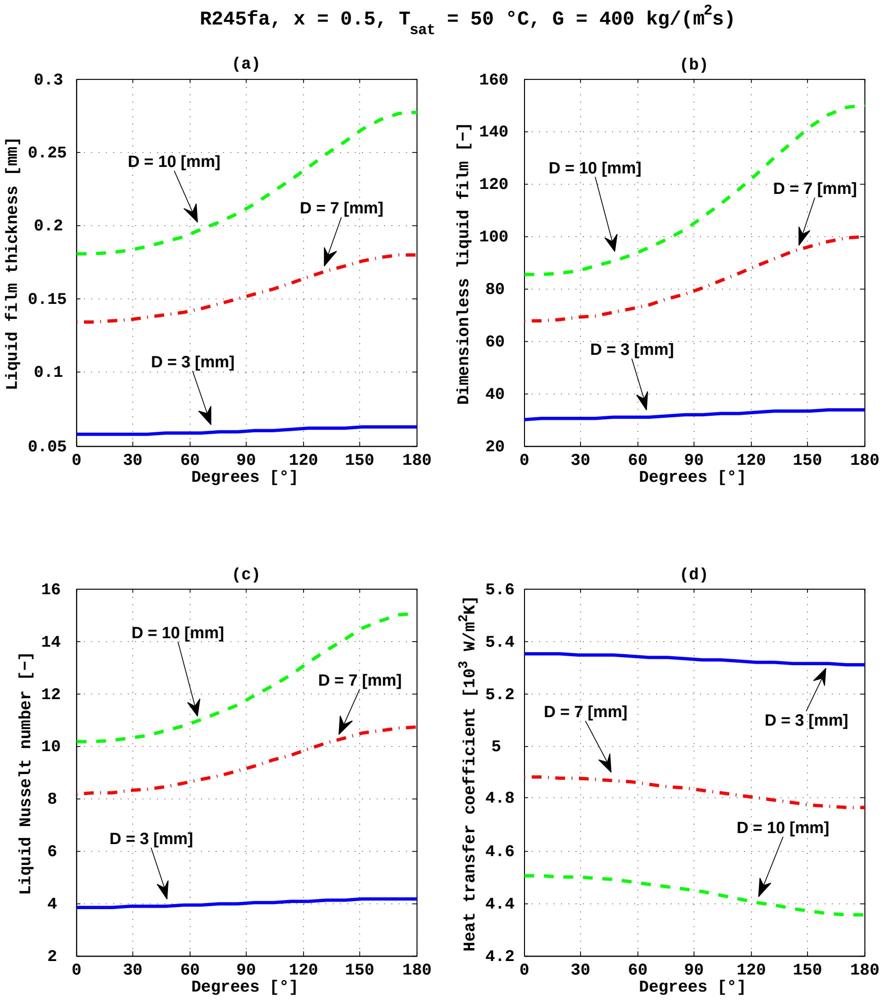

Figure 5.7: Influence of the channel diameter on (a) liquid film distribution, (b) dimensionless liquid film thickness, (c) liquid Nusselt number and (d) local heat transfer coefficient.

- The share of the turbulent core's thermal resistance decreases as the vapour quality increases. It seems that the value of vapour quality, at which the heat transfer coefficient shows a maximum, corresponds nearly to the disappearance of the turbulent core's thermal resistance.

The decrease of the heat transfer coefficient toward to the tube bottom has been found in all the conditions analysed in this study, and the behaviour seems to be in contrast to the data of Zimmerman et al. [29]. It results that, whereas the conditions and the thermodynamic properties promote the turbulence at the tube bottom in air-water flows, the conduction dominates in refrigerants flows. Therefore, the effect of the liquid film stratification on the heat transfer coefficient differs varying the working fluids and operational conditions.

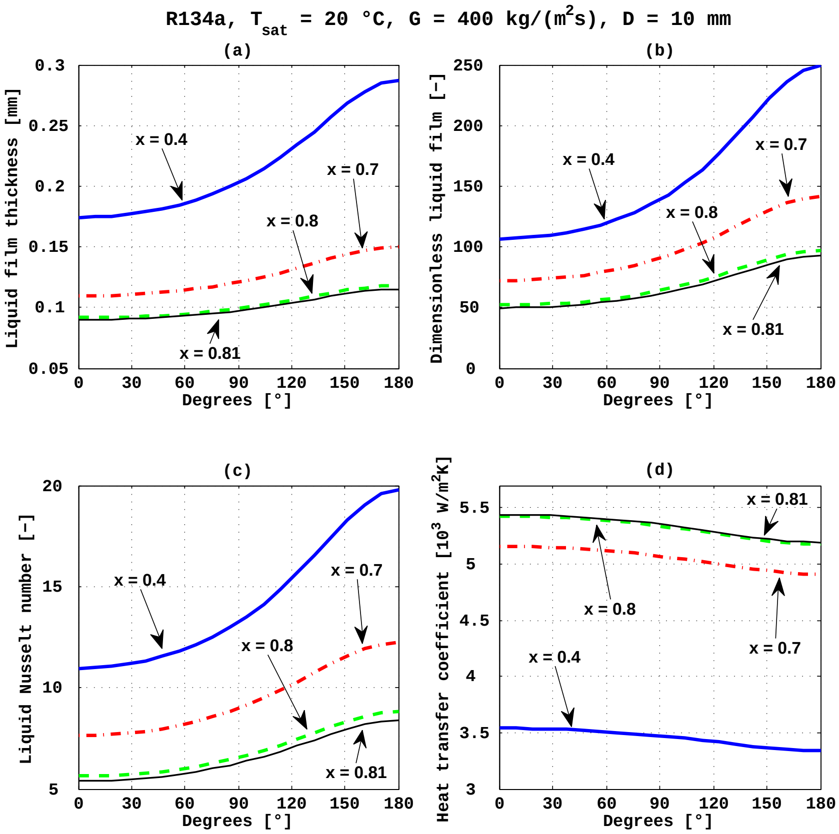

Figure 5.8: Influence of the vapour quality on (a) liquid film distribution, (b) dimensionless liquid film thickness, (c) liquid Nusselt number and (d) local heat transfer coefficient.

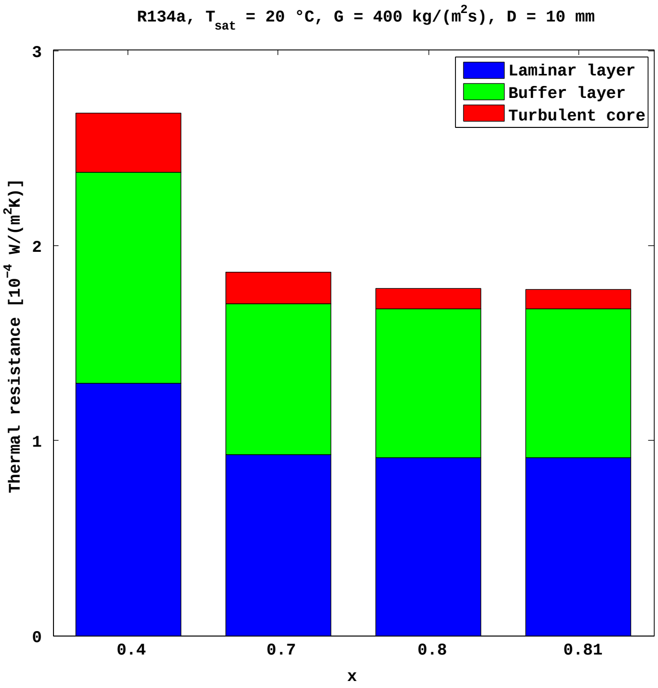

Figure 5.9: Thermal resistances distribution for laminar sublayer, buffer layer and turbulent core on varying the vapour quality.

Chapter 6

CONCLUSIONS

The fluid mechanics and heat transfer in two-phase flow has always been a challenging matter. The consequences of the interaction between the liquid and the vapour phases provide the reasons for the application in a wide field of fluid systems. In the present thesis, the characterization of the liquid film distribution in horizontal two-phase annular flow has been investigated in order to understand its effect on the pressure drop and the heat transfer coefficient. This topic may be very important in the design of heat exchangers involved by two-phase flows with significant liquid film stratification. The study yielded the following remarks:

- In literature, the studies concerning the liquid film distribution in annular flow are several. Direct Navier Stokes (DNS) is the most accurate method, since it can take complex phenomena into account, such as disturbance waves, but it requires great computational effort. Correlations for the liquid film distribution is easy to use, but it is valid in a narrow range of operational conditions and working fluids. A new method able to predict the liquid film distribution in annular flow is needed, which can hold simultaneously a satisfactory accuracy and a moderate computational effort.

- The modelling of the liquid film in horizontal annular flow has still some questions unanswered. In order to sustain the liquid film, the gravitational force has to be counterbalanced. It is not straightforward to determine which force is main responsible to this feature. It is evident that more experimental and theoretical investigations are needed to this feature for the purpose to define a more accurate and general model.

- A new two-dimensional model has been proposed in order to predict the liquid film distribution. Such a model resolves the mass and the momentum equations on each phase, with the aid of proper correlations for the liquid-wall shear stress and the interfacial shear stress. The main assumptions, on which the model is based, are the smoothness o the liquid-vapour interface and the absence of entrained liquid droplets.

- The two-dimensional model has been validated against an experimental database on pressure drop and on liquid film thickness. The pressure drop database is endowed with the following ranges of operational conditions and working fluids: channel diameter $0.517 - 10.85$ mm; fluids R134a, R1234yf, R410A, carbon dioxide; mass flux $300 - 2000$ $kg/(m^2 s)$; saturation temperature $5 - 30$°C; vapour quality $0.08 - 0.8$. In regard to the liquid film database, the compared measurements are allocated among the following limits: $8.15 - 12.3$ mm; fluid air-water; liquid superficial velocity $0.16 - 0.4$ m/s; vapour superficial velocity $10 - 40$ m/s; pressure 100 kPa. The comparison between the two-dimensional model and the experimental database resulted to be satisfactory.

- The liquid film thickness prediction results to be only reliable for relatively low pressure drop conditions. As a matter of fact, the amount of entrainment rate becomes largely significant in high pressure drop flows, in conflict with the model assumptions. This behaviour is confirmed by a comparison between the two-dimensional model and a pressure drop correlation.

- It results that the more the gravitational acceleration, the more the pressure drop. The reason for such a behaviour has to be found in the phenomenological nature of the interfacial shear stress. The increase of the gravity force causes an increase in the cross-sectional average value of the liquid film thickness, which, in turn, produces an accretion of the interfacial roughness. However, the influence of the gravitational acceleration is only significant for low pressure drop flows.

- The tangential variation of the heat transfer coefficient in the liquid film proves to be negative in the conditions analysed previously. This behaviour is due to the mainly conductive characteristic of the heat transfer, in contrast to experimental data for air-water flows present in literature. The turbulent core provides a negligible thermal resistance, in contrast to the laminar sublayer's and buffer layer's. As long as the stratification occurs, the increase of the film thickness toward the tube bottom causes an increase of the thermal resistance.

- Such a variation of the heat transfer coefficient become more relevant in high thermal resistance conditions, namely for higher saturation temperature and/or larger channel diameter. However, the comparison between the two-dimensional model and a heat transfer coefficient correlation for condensing flow shows an good agreement.

The two-dimensional model proposed in this study is a starting point in order to better approach at the heat exchanger design involved by horizontal two-phase annular flow. The model may be improved further taking the entrainment and the deposition of liquid droplets into account, and using a more accurate model of turbulence for the heat transfer. However, a wider validation against experimental data on liquid film thickness and heat transfer coefficient is needed.

Bibliography

[1] IEA. *Key World Energy Statistic.* 1

[2] B.F. Tchanche, M. Ptrissans, and G. Papadakis. Heat resources and organic rankine cycle machines. *Renewable and Sustainable Energy Reviews*, 39(0):1185 – 1199, 2014. 1, 1

[3] T.C. Hung, T.Y. Shai, and S.K. Wang. A review of organic rankine cycles (orcs) for the recovery of low-grade waste heat. *Energy*, 22(7):661 – 667, 1997. 1

[4] A. Borsukiewicz-Gozdur and W. Nowak. Maximising the working fluid flow as a way of increasing power output of geothermal power plant. *Applied Thermal Engineering*, 27(1112):2074 – 2078, 2007. 1

[5] H. Chen, D.Y. Goswami, and E.K. Stefanakos. A review of thermodynamic cycles and working fluids for the conversion of low-grade heat. *Renewable and Sustainable Energy Reviews*, 14(9):3059 – 3067, 2010. 1

[6] A.I. Papadopoulos, M. Stijepovic, and P. Linke. On the systematic design and selection of optimal working fluids for organic rankine cycles. *Applied Thermal Engineering*, 30(67):760 – 769, 2010. 1

[7] S. Quoilin, S. Declaye, B.F. Tchanche, and V. Lemort. Thermo-economic optimization of waste heat recovery organic rankine cycles. *Applied Thermal Engineering*, 31(1415):2885 – 2893, 2011. 1

[8] M. Aneke, B. Agnew, C. Underwood, H. Wu, and S. Masheiti. Power generation from waste heat in a food processing application. *Applied Thermal Engineering*, 36(0):171 – 180, 2012. 1

[9] C. He, C. Liu, H. Gao, H. Xie, Y. Li, S. Wu, and J. Xu. The optimal evaporation temperature and working fluids for subcritical organic rankine cycle. *Energy*, 38(1):136 – 143, 2012. 1

[10] J. Bao and L. Zhao. A review of working fluid and expander selections for organic rankine cycle. *Renewable and Sustainable Energy Reviews*, 24(0):325 – 342, 2013. 1

[11] F. Cataldo, R. Mastrullo, A.W. Mauro, and G.P. Vanoli. Fluid selection of organic rankine cycle for low-temperature waste heat recovery based on thermal optimization. *Energy*, 72(0):159 – 167, 2014. 1

[12] N. Kattan, J.R. Thome, and D. Favrat. Flow boiling in horizontal tubes: Part 1 - development of a diabatic two-phase flow pattern map. *Journal of Heat Transfer*, 120(1):140–146, 1998. 1

[13] O. Zurcher, D. Favrat, and J.R. Thome. Development of a diabatic two-phase flow pattern map for horizontal flow boiling. *International Journal of Heat and Mass Transfer*, 45(2):291 – 301, 2002. 1

[14] J. El Hajal, J.R Thome, and A. Cavallini. Condensation in horizontal tubes, part i: two-phase flow pattern map. *International Journal of Heat and Mass Transfer*, 46(18):3349 – 3363, 2003. 1

[15] L. Wojtan, T. Ursenbacher, and J.R. Thome. Investigation of flow boiling in horizontal tubes: Part i - a new diabatic two-phase flow pattern map. *International Journal of Heat and Mass Transfer*, 48(14):2955 – 2969, 2005. 1, 1

[16] L. Wojtan, T. Ursenbacher, and J.R. Thome. Investigation of flow boiling in horizontal tubes: Part ii - development of a new heat transfer model for stratified-wavy, dryout and mist flow regimes. *International Journal of Heat and Mass Transfer*, 48(14):2970 – 2985, 2005. 1

[17] R. Mastrullo, A.W. Mauro, J.R. Thome, D. Toto, and G.P. Vanoli. Flow pattern maps for convective boiling of {CO2} and {R410A} in a horizontal smooth tube: Experiments and new correlations analyzing the effect of the reduced pressure. *International Journal of Heat and Mass Transfer*, 55(56):1519 – 1528, 2012. 1

[18] S.-M. Kim and I. Mudawar. Universal approach to predicting saturated flow boiling heat transfer in mini/micro-channels part i. dryout incipience quality. *International Journal of Heat and Mass Transfer*, 64(0):1226 – 1238, 2013. 1

[19] R. Charnay, J. Bonjour, and R. Revellin. Experimental investigation of r-245fa flow boiling in minichannels at high saturation temperatures: Flow patterns and flow pattern maps. *International Journal of Heat and Fluid Flow*, 46(0):1 – 16, 2014. 1

[20] J.G. Collier and J.R. Thome. *Convective Boiling and Condensation*. Oxford engineering science series. Clarendon Press, 1996. 1, 1, 2.2, 2.2.1, 4.1

[21] G.B. Wallis. *One-dimensional two-phase flow*. McGraw-Hill, 1969. 1, 2.2, 2.2.1, 2.2.1

[22] G.F. Hewitt. *Annular Two-Phase Flow*. Elsevier Science, 2013. 1

[23] T. Hanratty. *Two-Phase Annular and Dispersed Flow*. Pergamon Press, 1985. 1

[24] P.B. Whalley. *Boiling, condensation, and gas-liquid flow.* Oxford engineering science series. Clarendon Press, 1987. 1, 2.1.1

[25] A. Bar-Cohen, Z. Ruder, and P. Griffith. Circumferential wall temperature variations in horizontal boiler tubes. *International Journal of Multiphase Flow*, 9(1):1 – 12, 1983. 1

[26] A. Bar-Cohen, Z. Ruder, and P. Griffith. Thermal and hydrodynamic phenomena in a horizontal, uniformly heated steam-generating pipe. *Journal of Heat Transfer*, 109(3):739–745, 1987. 1

[27] S. Jayanti and G.F. Hewitt. Hydrodynamics and heat transfer in wavy annular gas-liquid flow: a computational fluid dynamics study. *International Journal of Heat and Mass Transfer*, 40(10):2445 – 2460, 1997. 1

[28] G. Hetsroni, D. Mewes, C. Enke, M. Gurevich, A. Mosyak, and R. Rozenblit. Heat transfer to two-phase flow in inclined tubes. *International Journal of Multiphase Flow*, 29(2):173 – 194, 2003. 1

[29] R. Zimmerman, M. Gurevich, A. Mosyak, R. Rozenblit, and G. Hetsroni. Heat transfer to airwater annular flow in a horizontal pipe. *International Journal of Multiphase Flow*, 32(1):1 – 19, 2006. 1, 5.2

[30] G.F. Hewitt D.G. Owen. An improved annular two-phase flow model. In *3rd International Conference on Multi-Phase Flow.* 2.1.1

[31] E.T. Hurlburt and T.A. Newell. Prediction of the circumferential film thickness distribution in horizontal annular gas-liquid flow. *Journal of Fluids Engineering, Transactions of the ASME*, 122(2):396–402, 2000. cited By 26. 2.1.1, 2.1.2, 2.1.3, 2.4

[32] T.A. Shedd. Two-phase internal flow: Toward a theory of everything. *Heat Transfer Engineering*, 34(5-6):420–433, 2013. 2.1.1, 2.2.1

[33] F. Dobran. Hydrodynamic and heat transfer analysis of two-phase annular flow with a new liquid film model of turbulence. *International Journal of Heat and Mass Transfer*, 26(8):1159 – 1171, 1983. 2.1.1

[34] F. Dobran. Heat transfer in an annular two-phase flow. *Journal of Heat Transfer*, 107(2):472–476, 1985. 2.1.1

[35] A. Cioncolini, J.R. Thome, and C. Lombardi. Algebraic turbulence modeling in adiabatic gasliquid annular two-phase flow. *International Journal of Multiphase Flow*, 35(6):580 – 596, 2009. 2.1.1, 2.4

[36] P.G. Kosky. Thin liquid films under simultaneous shear and gravity forces. *International Journal of Heat and Mass Transfer*, 14(8):1220 – 1224, 1971. 2.1.2

[37] M. Ishii and M.A. Grolmes. Inception criteria for droplet entrainment in two-phase concurrent film flow. *AIChE Journal*, 21(2):308–318, 1975. 2.1.2

[38] C. Berna, A. Escriv, J.L. Muoz-Cobo, and L.E. Herranz. Review of droplet entrainment in annular flow: Interfacial waves and onset of entrainment. *Progress in Nuclear Energy*, 74(0):14 – 43, 2014. 2.1.2, 2.1.2, 4.2.2

[39] J.C. Asali, T.J. Hanratty, and P. Andreussi. Interfacial drag and film height for vertical annular flow. *AIChE Journal*, 31(6):895–902, 1985. cited By 146. 2.1.2, 2.1.2, 2.2.1

[40] E.T. Hurlburt and T.A. Newell. Characteristics of refrigerant film thickness, pressure drop, and condensation heat transfer in annular flow. *HVAC and R Research*, 5(3):229–248, 1999. 2.1.2, 5.1

[41] P.S. Sacks. Measured characteristics of adiabatic and condensing single component two phase flow of regrigerant in a 0.377 inch diameter horizontal tube. In *Paper presented at the ASME winter annual meeting*. 2.1.2

[42] J.P. Wattelet. *Heat Transfer Flow Regimes of Refrigerants in Horizontal-Tube Evaporator*. PhD thesis, University of Illinois, Urbana-Champaign, 1994. 2.1.2

[43] M.K. Dobson. *Heat Transfer and Flow Regimes During Condensation in Horizontal Tubes*. PhD thesis, University of Illinois, Urbana-Champaign, 1994. 2.1.2

[44] T. Fukano and T. Furukawa. Prediction of the effects of liquid viscosity on interfacial shear stress and frictional pressure drop in vertical upward gas-liquid annular flow. *International Journal of Multiphase Flow*, 24(4):587 – 603, 1998. 2.1.2, 2.1.2, 2.2.1, 2.2.1, 3.2.2

[45] J.M. Rodriguez. *Numerical Simulation of Two-phase Annular Flow*. PhD thesis, Rensselaer Polytechnic Institute, New York, 2009. 2.1.2

[46] W.H. Henstock and T.J. Hanratty. The interfacial drag and the height of the wall layer in annular flows. *AIChE Journal*, 22(6):990–1000, 1976. 2.1.2, 2.2.1

[47] D.F. Tatterson, J.C. Dallman, and T.J. Hanratty. Drop sizes in annular gas-liquid flows. *AIChE Journal*, 23(1):68–76, 1977. 2.1.2

[48] T. Okawa, T. Kitahara, K. Yoshida, T. Matsumoto, and I. Kataoka. New entrainment rate correlation in annular two-phase flow applicable to wide range of flow condition. *International Journal of Heat and Mass Transfer*, 45(1):87 – 98, 2002. 2.1.2

[49] P.A. Roberts, B.J. Azzopardi, and S. Hibberd. The split of horizontal annular flow at a t-junction. *Chemical Engineering Science*, 52(20):3441–3453, 1997. 2.1.2

[50] D. Schubring and T.A. Shedd. Critical friction factor modeling of horizontal annular base film thickness. *International Journal of Multiphase Flow*, 35(4):389 – 397, 2009. 2.1.3, 2.2.1, 3.2.2

[51] A. Cioncolini and J.R. Thome. Liquid film circumferential asymmetry prediction in horizontal annular two-phase flow. *International Journal of Multiphase Flow*, 51(0):44 – 54, 2013. 2.1.3, 2.1.3

[52] A.W. Mauro, A. Cioncolini, J.R. Thome, and R. Mastrullo. Asymmetric annular flow in horizontal circular macro-channels: Basic modeling of liquid film distribution and heat transfer around the tube perimeter in convective boiling. *International Journal of Heat and Mass Transfer*, 77(0):897 – 905, 2014. 2.1.3

[53] L.B. Fore, S.G. Beus, and R.C. Bauer. Interfacial friction in gasliquid annular flow: analogies to full and transition roughness. *International Journal of Multiphase Flow*, 26(11):1755 – 1769, 2000. 2.2, 2.2.1, 2.2.1, 2.2.1, 2.2.1, 3.2.2

[54] E.O. Moeck. *Annular-dispersed two-phase flow and critical heat flux.* AECL. 2.2.1, 3.2.2

[55] J.C. Asali. *Entrainment in Vertical Gas-liquid Annular Flow.* PhD thesis, University of Illinois, Urbana-Champaign, 1984. 2.2.1

[56] L.B. Fore and A.E. Dukler. Droplet deposition and momentum transfer in annular flow. *AIChE Journal*, 41(9):2040–2046, 1995. 2.2.1

[57] L.B. Fore and A.E. Dukler. The distribution of drop size and velocity in gas-liquid annular flow. *International Journal of Multiphase Flow*, 21(2):137 – 149, 1995. 2.2.1

[58] T.A. Shedd A.C. Ashwood, D. Schubring. Direct measurements of liquid film roughness for the prediction of annular flow pressure drop. In *ECI International Conference on Boiling Heat Transfer.* 2.2.1

[59] D. Schubring and T.A. Shedd. Prediction of wall shear for horizontal annular air-water flow. *International Journal of Heat and Mass Transfer*, 52(12):200 – 209, 2009. 2.2.1, 2.2.1

[60] R.C. Bauer E.T. Hurlburt, L.B. Fore. A two zone model for vertical annular two-phase flow. In *Proceedings of ASME Fluids Engineering Division Summer Meeting Vol. 2.* 2.2.1

[61] D. Schubring and T.A. Shedd. A model for pressure loss, film thickness, and entrained fraction for gasliquid annular flow. *International Journal of Heat and Fluid Flow*, 32(3):730 – 739, 2011. 2.2.1, 2.2.1, 2.4, 3.2.2

[62] T. Hanratty J. Laurinat. *Studies of the Effects of Pipe Size on Horizontal Annular Two-Phase Flows.* PhD thesis, University of Illinois, Urbana-Champaign, 1982. 2.2.1

[63] S.V. Paras and A.J. Karabelas. Properties of the liquid layer in horizontal annular flow. *International Journal of Multiphase Flow*, 17(4):439 – 454, 1991. 2.2.1, 3.1.9

[64] A. Cioncolini and J.R. Thome. Algebraic turbulence modeling in adiabatic and evaporating annular two-phase flow. *International Journal of Heat and Fluid Flow*, 32(4):805 – 817, 2011. 2.3, 2.4

[65] T. Okawa, A. Kotani, I. Kataoka, and M. Naito. Prediction of critical heat flux in annular flow using a film flow model. *Journal of Nuclear Science and Technology*, 40(6):388–396, 2003. 2.4

[66] T. Okawa, A. Kotani, I. Kataoka, and M. Naitoh. Prediction of the critical heat flux in annular regime in various vertical channels. *Nuclear Engineering and Design*, 229(23):223 – 236, 2004. 2.4

[67] B.N. Kishore and S. Jayanti. A multidimensional model for annular gas-liquid flow. *Chemical Engineering Science*, 59(17):3577–3589, 2004. 2.4, 3.2.2

[68] V.M. Alipchenkov, R.I. Nigmatulin, S.L. Soloviev, O.G. Stonik, L.I. Zaichik, and Y.A. Zeigarnik. A three-fluid model of two-phase dispersed-annular flow. *International Journal of Heat and Mass Transfer*, 47(24):5323 – 5338, 2004. 2.4, 3.2.1, 3.2.2

[69] R. Revellin and J.R. Thome. A theoretical model for the prediction of the critical heat flux in heated microchannels. *International Journal of Heat and Mass Transfer*, 51(56):1216 – 1225, 2008. 2.4, 3.2.1

[70] A. Cioncolini, J.R. Thome, and C. Lombardi. Unified macro-to-microscale method to predict two-phase frictional pressure drops of annular flows. *International Journal of Multiphase Flow*, 35(12):1138 – 1148, 2009. 2.4

[71] Y. Whan Na and J.N. Chung. Two-phase annular flow and evaporative heat transfer in a microchannel. *International Journal of Heat and Fluid Flow*, 32(2):440 – 450, 2011. 2.4, 3.2.1, 3.2.2

[72] Y. Liu, J. Cui, and W.Z. Li. A two-phase, two-component model for vertical upward gasliquid annular flow. *International Journal of Heat and Fluid Flow*, 32(4):796 – 804, 2011. 2.4

[73] S.-M. Kim and I. Mudawar. Theoretical model for annular flow condensation in rectangular micro-channels. *International Journal of Heat and Mass Transfer*, 55(4):958 – 970, 2012. 2.4, 3.2.1, 3.2.2

[74] S.-M. Kim and I. Mudawar. Theoretical model for local heat transfer coefficient for annular flow boiling in circular mini/micro-channels. *International Journal of Heat and Mass Transfer*, 73(0):731 – 742, 2014. 2.4, 3.2.1, 3.2.2

[75] H. Li and H. Anglart. {CFD} model of diabatic annular two-phase flow using the eulerianlagrangian approach. *Annals of Nuclear Energy*, 77(0):415 – 424, 2015. 2.4

[76] R. Zhang, H. Liu, and M. Liu. A probability model for fully developed annular flow in vertical pipes: Prediction of the droplet entrainment. *International Journal of Heat and Mass Transfer*, 84(0):225 – 236, 2015. 2.4

[77] S. Jesseela and C.B. Sobhan. Numerical modeling of annular flow with phase change in a microchannel. *International Journal of Thermal Sciences*, 89(0):87 – 99, 2015. 2.4

[78] L.R. Williams. *Effect of Pipe Diameter on Horizontal Annular Two-Phase Flow.* PhD thesis, University of Illinois, Urbana-Champaign, 1990. 2.4

[79] J.E. Laurinat, T.J. Hanratty, and W.P. Jepson. Film thickness distribution for gas-liquid annular flow in a horizontal pipe. *PCH, PhysicoChemical Hydrodynamics*, 6(1-2):179–195, 1984. 2.4, 2.5

[80] T. Fukano and A. Ousaka. Prediction of the circumferential distribution of film thickness in horizontal and near-horizontal gas-liquid annular flows. *International Journal of Multiphase Flow*, 15(3):403 – 419, 1989. 2.4, 2.5

[81] Hua Sheng Wang and John W. Rose. Film condensation in horizontal microchannels: Effect of channel shape. *International Journal of Thermal Sciences*, 45(12):1205 – 1212, 2006. 2.4, 3.2.2

[82] S. Nebuloni and J.R. Thome. Numerical modeling of laminar annular film condensation for different channel shapes. *International Journal of Heat and Mass Transfer*, 53(1314):2615 – 2627, 2010. 2.4, 3.2.1, 3.2.2

[83] E. Da Riva, D. Del Col, S.V. Garimella, and A. Cavallini. The importance of turbulence during condensation in a horizontal circular minichannel. *International Journal of Heat and Mass Transfer*, 55(1314):3470 – 3481, 2012. 2.4, 3.2.1

[84] T.F. Lin, O.C. Jones Jr., R.T. Lahey Jr., R.C. Block, and M. Murase. Film thickness measurements and modelling in horizontal annular flows. *PCH, PhysicoChemical Hydrodynamics*, 6(1-2):197–206, 1984. 2.5

[85] A.G. Flores, K.E. Crowe, and P. Griffith. Gas-phase secondary flow in horizontal, stratified and annular two-phase flow. *International Journal of Multiphase Flow*, 21(2):207 – 221, 1995. 2.5, 3.1.9

[86] H.N. McManus Jr. R.S. Darling. Flow patterns in circular ducts with circumferential variation of roughness: a two-phase analog. In *Developments in Mechanics: Proceedings of the 11th Midwestern Mechanics Conference Vol. 5.* 2.5

[87] L.M. Portela R.F. Mudde R.V.A. Oliemans R.J. Belt, J.M.C. van t Westende. Direct numerical simulation of particle-driven secondary flow in turbulent horizontal pipe flows. In *11th Workshop on Two-Phase Flow Predictions*. 2.5

[88] C.G. Speziale. On turbulent secondary flows in pipes of noncircular cross-section. *International Journal of Engineering Science*, 20(7):863 – 872, 1982. 2.5

[89] T. W. F. Russell and D. E. Lamb. Flow mechanism of two-phase annular flow. *The Canadian Journal of Chemical Engineering*, 43(5):237–245, 1965. 2.5

[90] D. Butterworth and D.J. Pulling. *A Visual Study of Mechanisms in Horizontal, Annular, Air-water Flow*. AERE memorandum / M: AERE memorandum. Atomic Energy Research Establishment, 1972. 2.5

[91] S. Jayanti, G.F. Hewitt, and S.P. White. Time-dependent behaviour of the liquid film in horizontal annular flow. *International Journal of Multiphase Flow*, 16(6):1097 – 1116, 1990. 2.5

[92] B. Sutharshan, M. Kawaji, and A. Ousaka. Measurement of circumferential and axial liquid film velocities in horizontal annular flow. *International Journal of Multiphase Flow*, 21(2):193 – 206, 1995. 2.5, 3.1.9

[93] S. Jayanti and G.F. Hewitt. Response of turbulent flow to abrupt changes in surface roughness and its relevance in horizontal annular flow. *Applied Mathematical Modelling*, 20(3):244–251, 1996. 2.5

[94] T. Fukano and T. Inatomi. Analysis of liquid film formation in a horizontal annular flow by {DNS}. *International Journal of Multiphase Flow*, 29(9):1413 – 1430, 2003. 2.5

[95] J.M.C. van t Westende, R.J. Belt, L.M. Portela, R.F. Mudde, and R.V.A. Oliemans. Effect of secondary flow on droplet distribution and deposition in horizontal annular pipe flow. *International Journal of Multiphase Flow*, 33(1):67 – 85, 2007. 2.5, 3.1.9

[96] J.O. McCaslin and O. Desjardins. Numerical investigation of gravitational effects in horizontal annular liquidgas flow. *International Journal of Multiphase Flow*, 67(0):88 – 105, 2014. 2.5

[97] E. Kreyszig. *Differential Geometry*. Differential Geometry. Dover Publications, 1991. 3.1.3

[98] T. Hohne, T. Geissler, A. Bieberle, and U. Hampel. Numerical modeling of a horizontal annular flow experiment using a droplet entrainment model. *Annals of Nuclear Energy*, 77(0):351 – 360, 2015. 3.1.9

[99] S.W. Churchill. Friction-factor equation spans all fluid-flow regimes. *Chemical Engineering (New York)*, 84(24):91–92, 1977. cited By 448. 3.2.2

[100] R.K. Shah, A.L. London, T.F. Irvine, and J.P. Hartnett. *Laminar Flow Forced Convection in Ducts: A Source Book for Compact Heat Exchanger Analytical Data.* Advances in heat transfer: Supplement. Elsevier Science, 2014. 3.2.2

[101] R.J. Belt, J.M.C. Vant Westende, and L.M. Portela. Prediction of the interfacial shear-stress in vertical annular flow. *International Journal of Multiphase Flow*, 35(7):689 – 697, 2009. 3.2.2

[102] G. Lindfield and J. Penny. *Numerical Methods: Using MATLAB.* Elsevier Science, 2012. 4.1

[103] M. Padilla, R. Revellin, P. Haberschill, A. Bensafi, and J. Bonjour. Flow regimes and two-phase pressure gradient in horizontal straight tubes: Experimental results for hfo-1234yf, r-134a and r-410a. *Experimental Thermal and Fluid Science*, 35(6):1113 – 1126, 2011. 4.2.1

[104] R. Mastrullo, A.W. Mauro, A. Rosato, and G.P. Vanoli. Carbon dioxide heat transfer coefficients and pressure drops during flow boiling: Assessment of predictive methods. *International Journal of Refrigeration*, 33(6):1068 – 1085, 2010. 4.2.1

[105] R. Revellin and J.R. Thome. Adiabatic two-phase frictional pressure drops in microchannels. *Experimental Thermal and Fluid Science*, 31(7):673 – 685, 2007. 4.2.1

[106] C. Berna, A. Escriv, J.L. Muoz-Cobo, and L.E. Herranz. Review of droplet entrainment in annular flow: Characterization of the entrained droplets. *Progress in Nuclear Energy*, 79(0):64 – 86, 2015. 4.2.2

[107] A. Cioncolini and J.R. Thome. Entrained liquid fraction prediction in adiabatic and evaporating annular two-phase flow. *Nuclear Engineering and Design*, 243(0):200 – 213, 2012. 4.2.2

[108] Y. Luninski, D. Barnea, and Y. Taitel. Film thickness in horizontal annular flow. *The Canadian Journal of Chemical Engineering*, 61(5):621–626, 1983. 4.2.3

[109] M. Damsohn and H.-M. Prasser. High-speed liquid film sensor for two-phase flows with high spatial resolution based on electrical conductance. *Flow Measurement and Instrumentation*, 20(1):1 – 14, 2009. 4.2.4

[110] A.C. Ashwood, S.J. Vanden Hogen, M.A. Rodarte, C.R. Kopplin, D.J. Rodrguez, E.T. Hurlburt, and T.A. Shedd. A multiphase, micro-scale {PIV} measurement technique for liquid film velocity measurements in annular two-phase flow. *International Journal of Multiphase Flow*, 68(0):27 – 39, 2015. 4.2.4

[111] S.M. Ghiaasiaan. *Two-Phase Flow, Boiling, and Condensation: In Conventional and Miniature Systems.* Cambridge University Press, 2007. 5.1

[112] Y. Zhao, C.N. Markides, O.K. Matar, and G.F. Hewitt. Disturbance wave development in two-phase gas-liquid upwards vertical annular flow. *International Journal of Multiphase Flow*, 55(0):111 – 129, 2013. 5.1

[113] S.-M. Kim and I. Mudawar. Review of databases and predictive methods for pressure drop in adiabatic, condensing and boiling mini/micro-channel flows. *International Journal of Heat and Mass Transfer*, 77(0):74 – 97, 2014. 5.1

[114] S.-M. Kim and I. Mudawar. Review of databases and predictive methods for heat transfer in condensing and boiling mini/micro-channel flows. *International Journal of Heat and Mass Transfer*, 77(0):627 – 652, 2014. 5.2